Volume 57
Number 81
18 October 2021
Pages 10439–10648

ChemComm

Chemical Communications

rsc.li/chemcomm

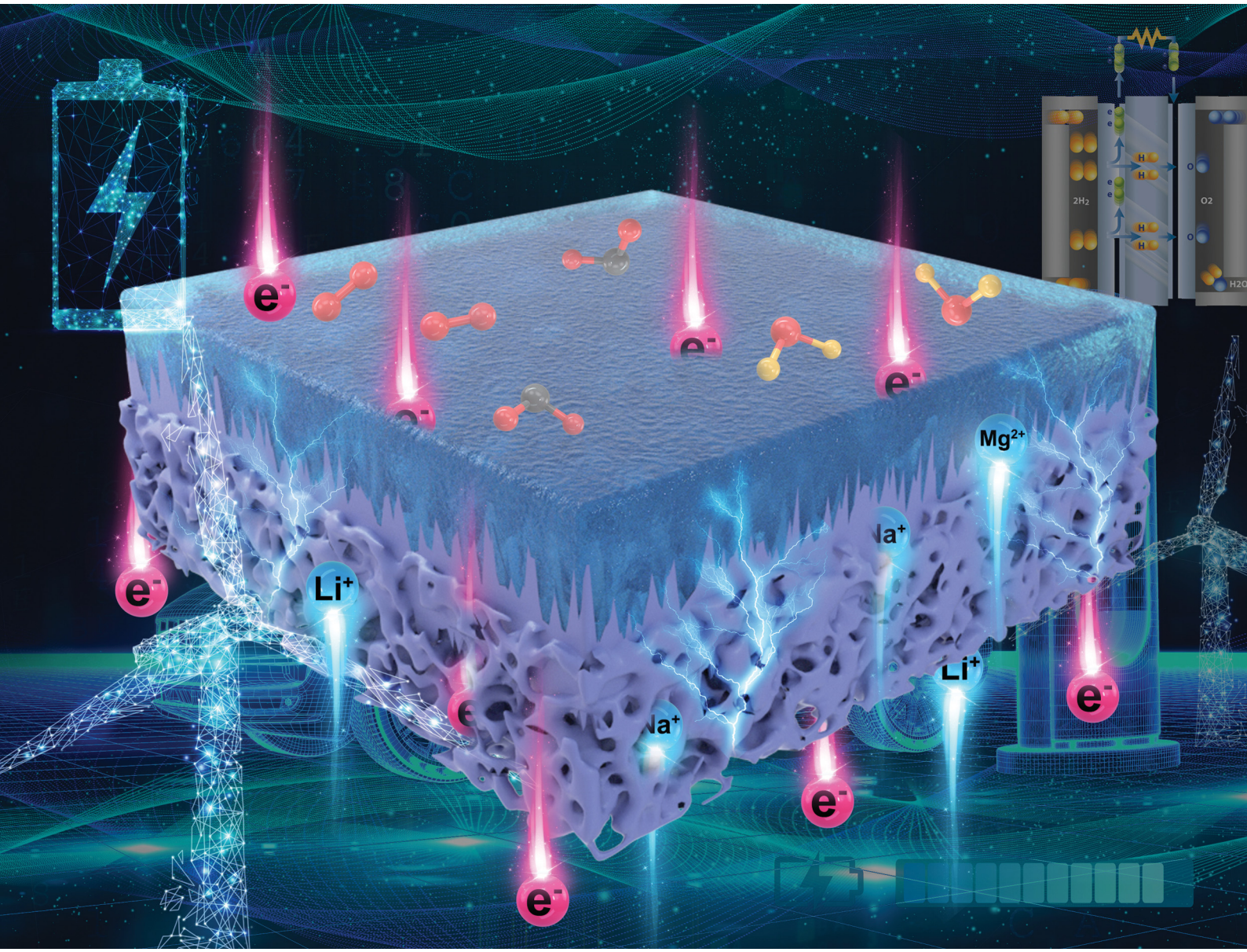

ISSN 1359-7345

ROYAL SOCIETY OF CHEMISTRY

FEATURE ARTICLE

Maoyu Wang and Zhenxing Feng

Interfacial processes in electrochemical energy systems

ChemComm

ROYAL SOCIETY OF CHEMISTRY

FEATURE ARTICLE

Cite this: *Chem. Commun.*, 2021, **57**, 10453

Interfacial processes in electrochemical energy systems

Maoyu Wang and Zhenxing Feng *

Received 31st March 2021,
Accepted 16th August 2021

DOI: 10.1039/d1cc01703a

rsc.li/chemcomm

Electrochemical energy systems such as batteries, water electrolyzers, and fuel cells are considered as promising and sustainable energy storage and conversion devices due to their high energy densities and zero or negative carbon dioxide emission. However, their widespread applications are hindered by many technical challenges, such as the low efficiency and poor long-term cyclability, which are mostly affected by the changes at the reactant/electrode/electrolyte interfaces. These interfacial processes involve ion/electron transfer, molecular/ion adsorption/desorption, and complex interface restructuring, which lead to irreversible modifications to the electrodes and the electrolyte. The understanding of these interfacial processes is thus crucial to provide strategies for solving those problems. In this review, we will discuss different interfacial processes at three representative interfaces, namely, solid–gas, solid–liquid, and solid–solid, in various electrochemical energy systems, and how they could influence the performance of electrochemical systems.

Introduction

With the increasing demand for energy resources and awareness of environmental problems, the development of sustainable energy devices has become the main effort in recent decades.[1–3] Electrochemical energy systems (EESs), such as batteries, fuel cells, and water electrolyzers, have been emerging as promising candidates for green devices due to their high energy density and low environmental pollution.[4–6] However, there are still many technical challenges in these EESs, which hamper their large-scale applications.[7,8] For example, to improve the energy density of current lithium–ion batteries (LIBs), the use of lithium metal as the anode is necessary, but the dendrite formation at the anode–electrolyte interface is a severe problem in batteries that use either solid-state or liquid electrolytes, resulting in safety issues, limited voltage window, and poor cyclability.[9–11] In LIBs, the electrode–electrolyte interphase (EEI) is treated as one of the critical elements to improve the performance of batteries.[9–11] Luchkin *et al.* reported that the performance and cyclability of LIBs strongly depend on the formation of passivation interphase layers.[12] Also, Suo *et al.* demonstrated that the EEI could block the electron transfer and only allow ion transfer to expand the voltage window of aqueous batteries.[13] Similarly, hydrogen fuel cells, which convert the chemical energy stored in hydrogen to electricity with no carbon emission, and electrolyzers, which split water to produce hydrogen and oxygen, suffer from the sluggish kinetics of the oxygen reduction reaction (ORR) and oxygen evolution reaction (OER),[14–17] respectively. The implementation of catalysts at the electrode–electrolyte interfaces in these energy conversion devices is essential to improve the surface reaction kinetics, thus helping achieve high efficiency for the whole system.[18–20] Hong *et al.* showed that the oxygen adsorption and dissociation on the electrode surface are important for improving the electrocatalyst function.[21] Clearly, all these studies have indicated that interfaces are critical components and the processes at these interfaces can significantly influence the performance of EESs. Therefore, to design next-generation EESs, it is necessary to conduct fundamental research at these interfaces and understand the connections between the interfacial processes and the performance of the device. In this Feature Article, we will go over and summarize the current progress in studies of interfacial processes in different EESs.

There are several different types of interfacial processes which can be categorized based on the effects on interfaces. The simplest one only involves the electron or charge transfer (Fig. 1a), which can take place on the electrocatalyst surfaces but may not be desired in most electrode–electrolyte interfaces in EESs, as electrons should be only allowed through outside wires. Only ionic transfer is preferred at the electrode–electrolyte interfaces (Fig. 1b). For example, Wang *et al.* reported a new type of aqueous battery electrolyte reacting with a Li anode to form a stable EEI, which would limit the electron transfer and allow Li ion transfer to expand the battery voltage window.[22] Different from the electron transfer, ions have a relatively large size compared to electrons, which may cause structural changes at these interfaces. For intercalation type batteries

School of Chemical, Biological, and Environmental Engineering, Oregon State University, Corvallis, Oregon, USA. E-mail: zhenxing.feng@oregonstate.edu

This journal is © The Royal Society of Chemistry 2021

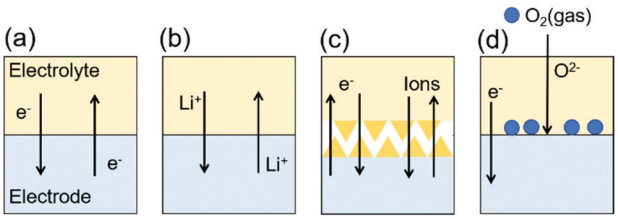

Fig. 1 Interfacial process schematic for (a) electron (charge) transfer, (b) ionic transfer, (c) surface reconstruction and (d) surface adsorption/desorption. The Li ion and oxygen electroreduction reaction is shown as an example.

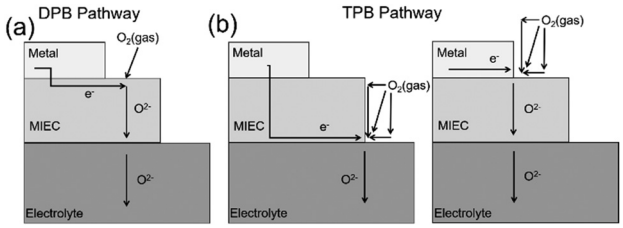

Fig. 2 A schematic of the reaction pathways involving the (a) DPB and (b) TPB through metals, MIEC and electrolytes. The ORR is shown as an example.

such as LIBs, the intercalation of Li^+ may or may not result in any interfacial modifications.[23] However, such interfaces always change in conversion-type batteries such as lithium–sulfur batteries.[24] The third case involves both electron and ion transfer (Fig. 1c), which can lead to significant surface reconstruction at the interface and it is the most common interfacial process (*e.g.*, the formation of the solid–electrolyte interphase, or SEI).[25–27] The fourth case is the surface adsorption/desorption, which is well known in electrochemical systems that involve gas or reaction intermediates such as electrocatalyst surfaces in fuel cells and water electrolyzers.[28–30] Similar to the ion transfer reaction, the surface adsorption/desorption may result in surface reconstruction. For example, Wygant *et al.* pointed out that most transition metal carbides, pnictides, and chalcogenides such as FeS, CoS, and NiS would undergo surface reconstruction when adsorbing oxygen ions during the OER, but some transition metal chalcogenides such as NiSe may not experience a surface structure change.[31] In this Feature Article, we will go over the recent progress in solid–gas, solid–liquid, and solid–solid interfaces in different electrochemical energy systems to illustrate the corresponding interfacial processes. We will also briefly discuss the related characterization techniques, particularly *in situ* and *operando*, which are suitable to probe the complex changes.

Solid–gas interface

A solid–gas interface (SGI) commonly exists in chemical reactions, particularly in heterogeneous catalysis, where the molecules are absorbed on the catalyst surfaces and subsequently react and desorb. Research in surface science has been diversely developed by studying the restructuring and changes at the SGI in catalysis. In addition to understanding such processes in either bulk powders or nanoparticles,[32–38] single crystal and thin films are widely used as the model systems to study the chemical reactions at the SGI through numerous surface-sensitive techniques (*e.g.*, X-ray, electron microscopy, *etc.*), with great insights obtained.[39–50] In electrochemical devices, such interfaces can be found in gas-breathing components. For example, the fuel cell cathode and anode that involve gas adsorption and charge transfer are one type of SGI. Metal–air batteries also need to accommodate air or oxygen diffusion through the corresponding electrode, thus forming a SGI. One of the best examples of SGIs could be the anode and cathode of solid oxide fuel cells (SOFCs),[51–53] which are operated at elevated temperatures (500–1000 °C) to react with hydrogen and oxygen, respectively, and is a potential alternative to conventional fire-power plants for electricity generation owing to high efficiency and low carbon emission of SOFCs.[51,54,55] A typical SOFC process involves the electrochemical reduction of oxygen molecules over the cathode to oxygen ions, and the diffusion of oxygen ions through the electrolyte and then to the anode for the reaction with hydrogen. The sluggish ORR kinetics at the cathode and poor oxygen ionic conductivity are two major issues that affect the performance of SOFCs and hinder their large-scale utilization.[51,54,55] Researchers have found that if the cathode thickness is less than the critical thickness (L_c) that is defined by the ratio of diffusion coefficient (D) and surface exchange coefficient (k),[56,57] the rate limiting step is the ORR at the surfaces, otherwise the bulk diffusion limits the whole reaction. Clearly these two processes are associated with the SGI, and Fig. 2 illustrates three scenarios which can be further categorized as the dual phase boundary (DPB) and triple phase boundary (TPB).[58] The following discussion will be focused on the cathode interfaces of SOFCs as examples.

In a DPB, the oxygen gases interact with the solid cathode or catalyst interfaces and go through the following processes: the oxygen molecule is directly absorbed on the mixed ionic electron conductor (MIEC) and disassociates to oxygen atoms or is directly reduced to oxygen ions, and then the oxygen ions diffuse through the electrolyte to the anode (Fig. 2a).[58] These adsorption and diffusion steps may lead to some surface structure modification or degradation. The oxygen adsorption and dissociation can be facilitated by either the cathode itself or additionally added catalyst materials, and the surface restructuring or degradation directly influence both the performance and durability of SOFCs. Therefore, controlling the undesired side reaction and inhibiting the surface degradation at the SGI is one promising way to improve the performance of SOFCs. An effective means is to modify the surface composition or coat/decorate a thin layer that prevents restructuring. For example, Pang *et al.* found that the optimization of surface composition of $La_{0.5}Ba_{0.5}CoO_x$ by creating Ba-deficiency can suppress the formation of a segregation layer, decrease the oxide ion diffusion barrier, and stabilize the crystal structure for better ORR durability and activity.[59] Moreover, Yang *et al.*

 This journal is © The Royal Society of Chemistry 2021

reported that $SrFe_{0.85}Ti_{0.1}Ni_{0.05}O_x$ decorated with NiO nanoparticles demonstrated better ORR activity than the benchmark cobalt based $Ba_{0.5}Sr_{0.5}Co_{0.8}Fe_{0.2}O_x$, and these NiO nanoparticles were treated as the important components to enhance the ORR performance.[60] Li *et al.* also demonstrated that the Co_3O_4 decorated $LaSrFeO_3$ surface will improve the surface ORR kinetics by changing the charge-transfer processes and increasing the surface oxygen exchange coefficient. Note that not all surface layers can prevent the surface restructuring and/or enhance the ORR activities. Shao-Horn's group showed that the surface decoration of $La_{0.8}Sr_{0.2}CoO_{3-\delta}$ with Sr composition (*e.g.*, SrO) can enhance the surface exchange coefficient and ORR activity, while "La"- and "Co"-decorations lead to no change of the ORR.[61] These studies have successfully confirmed that the surface composition and structure are important for the ORR kinetics, and similar strategies have been applied in battery research for surface coating on cathode materials to improve their stability and performance,[62] which will be illustrated in detail later. However, these studies have not provided deep insights into how surface composition or structure would change the reaction kinetics. Besides reports showing the effectiveness of surface coating on a DPB for the improvement of solid–gas interfacial processes, it is more important to figure out the physical origins for such enhancements or changes at the SGI.

To better understand this interfacial phenomenon in a DPB, Rupp *et al.* used real-time *in situ* electrochemical impedance spectroscopy (EIS) to monitor the oxygen reduction processes during surface modification of the $LaSrCoO_x$ (LSC) cathode, which shows excellent activity for the ORR but poor durability.[7] To find out the potential reason causing these degradations, they measured the surface exchange resistance and coefficient when growing the LSC with tiny amounts of SrO by pulsed laser deposition.[7] They found that SrO would lead to the deactivation of the LSC and Co adding will (re-)active the LSC.[7] The surface exchange resistance would increase and the surface exchange coefficient would decrease with more Sr decorated surfaces, but the Co showed an opposite trend to the Sr.[7] Moreover, the La decorated surface would not affect the surface exchange resistance and coefficient a lot.[7] These results indicate that Co atoms are the active sites for the ORR, and the decomposition of the LSC will lose Co atoms on the surface, which resulted in the deactivation of the LSC.[7] This finding seems to contradict other results which show that the Sr enrichment in the surface actually benefits the surface ORR.[61,63,64] To clarify these differences, the Adler group utilizes linear and non-linear impedance analysis on several gas–solid interfaces of LSC thin films including $La_{0.8}Sr_{0.2}CoO_{3-\delta}$ and $La_{0.6}Sr_{0.4}CoO_{3-\delta}$ under different partial oxygen pressures (Fig. 3a–c),[65,66] and revealed that these surfaces still obey a dissociative adsorption rate law despite substantial changes in the local properties. The enhancement caused by surface decoration or additional layer is primarily due to differences in the local thermodynamic properties rather than a shift in the reaction mechanism, which clarifies some debates in the literature arguing the unique properties of surface layers. Besides the electrochemical

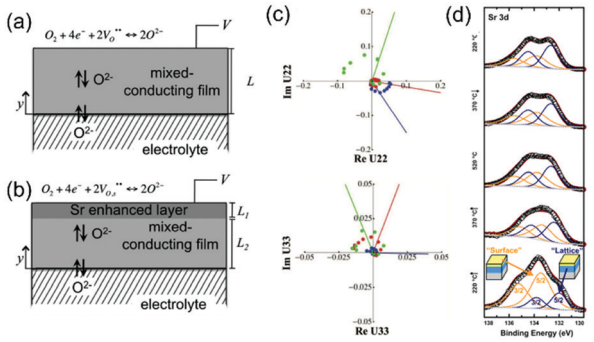

Fig. 3 Schematic illustrating the two possible distributions of the Sr dopant within the LSC thin film: (a) uniform cation distribution, and a (b) two-layer model in which the Sr/La ratio is enhanced within a layer of thickness of L1 near the gas-exposed surface.[65] (c) Measured 2nd and 3rd order harmonic response coefficients $U_{2,2}$ and $U_{3,3}$ for the 45-nm film tested at 520 °C and p_{O2} = 1.0 atm (blue), 0.1 atm (red) and 0.01 atm (green). (d) Sr 3d AP-XPS spectra of 90-nm LSC collected during the first heating.[69]

methods for mechanistic studies, several synchrotron X-ray characterization methods have also been extensively applied to study gas–solid interfaces in electrochemical devices, particularly SOFCs. Considering the surface sensitivity, X-ray photoelectron spectroscopy (XPS), especially ambient-pressure XPS (AP-XPS), is the primary choice for *in situ* investigations. This *in situ* characterization method was performed under various oxygen partial pressures with heating and applied voltages, truly mimicking the real operation conditions for electrochemical devices. Such studies have successfully coupled surface composition changes with heating (Fig. 3d) and applied voltages.[64,67,68] The reversible surface compositional changes under operating conditions are correlated with the role of corresponding elements in promoting the ORR and contribute to the stability of the gas–solid interfaces for long term run,[64,68] while some irreversible composition and structural changes at the initial cycles are believed to be the activation processes of SGIs that induce the local properties for subsequent ORR activity enhancement.[69] These *in situ* studies at the atomic-scale correlate the Sr composition changes with the enhanced ORR activity in thin film cathodes of SOFCs: the Sr enrichment in the crystal lattice (so-called coherent Sr) is beneficial for oxygen incorporation and thus the ORR and incoherent Sr particles on thin film surfaces are detrimental to solid–gas processes. In addition to experimental characterization methods, the theoretical calculations are also critical to connect the structural and composition changes with the performance of electrochemical devices, especially helpful in revealing the charge-transfer processes and adsorption power of molecules at the SGI with respect to surface oxygen exchange.[70] In theory, one can selectively study the influence of a specific factor on the SGI. For example, Xu *et al.* carried out a theoretical simulation to investigate the adsorption and dissociation of oxygen on different Co_3O_4 planes, which could guide the finding of suitable crystal orientation for the best ORR kinetics.[71] They pointed out that the Co_3O_4 (001) plane has the smallest oxygen

adsorption (−1.905 eV) and dissociation energies (1.69 eV) compared with (110) and (111) planes. Based on the guidance from the theoretical simulation, Co_3O_4 nano-cubes with (001) planes are exposed to the surface and applied in the cathode of SOFCs,[71] showing the best ORR performance among different crystal orientations.

Compared with the relatively simple reaction process in a DPB, the TPB involves more complex interfacial processes: the oxygen molecules are adsorbed and reduced at the interface of the solid electrocatalyst and electrolyte, which is the solid–solid–gas interface (SSGI) (Fig. 2b).[58] Like a DPB, the surface composition and microstructure affect the oxygen adsorption and dissociation, thus determining the fuel cell performance and cyclability. Chen *et al.* demonstrated a conformal CoO_x layer deposited on $(La_{1-x}Sr_x)MnO_3$ (LSM) and yttria stabilized zirconia (YSZ) backbones would improve the ORR kinetics.[72] Previously, a surface CoO_x layer was deposited on the cathode or catalyst surface (*e.g.*, DPB) only to improve the catalytic activity, but here they introduced it on both the cathode electrocatalyst and electrolyte, which formed a newly added triple phase boundary.[72] These new TBPs, which involve the solid electrode–electrolyte interface different from the DPB, reduced the polarization resistance dramatically and accelerated the oxygen diffusion to promote the ORR kinetics.[72] Studies have also suggested that the length, density, width, and the connection of the TPB are important microstructural metrics to assess the performance and durability of SOFCs,[73–78] as these parameters can affect the available active sites for the ORR. For instance, the TPB with a greater length has more available reaction sites. Cai *et al.* reported a simple laser microprocess to improve the performance of SOFCs by changing the TPB structure with an extended length. From their scanning electron microscopy (SEM) images, they showed that the laser micro-processing could create dimples and small cracks, improving the connectivity between the electrolyte and electrocatalyst and the interfacial area. These changes resulted in a remarkable decrease of both ohmic and polarization resistance, subsequently increasing the cell power density up to 58%.[79] Similarly Jeong *et al.* demonstrated that sputtered ultrathin platinum–gadolinium doped ceria (GDC) cermet interlayers on the cathode side of the electrolyte increased the triple phase boundary density and enhanced the reaction kinetics for the ORR.[80] Those examples prove that the microstructures of the TPB (*e.g.*, density and length) are strongly linked to the TPB properties. Based on such conclusions, Zhang *et al.* used a three-dimensional (3D) microstructure simulation to predict the influence of the microstructure (volume fractions of constituents, particle size, shape, and thickness) of the TPB on the performance of SOFCs.[78] The simulations suggested that the greater porosity above 10% and below 35% of the TPB could lead to the best stability and performance. Both constituents (electrolyte and electrode) having a volume fraction of above 30% would have more than 87% active TPB. Their results also showed that reducing the thickness of a composite cathode could improve the TPB activity and using non-equiaxed particles increase the connectivity and thus reduce the percolation threshold.[78] Besides the cathode side, the TPB is also important at the anode side. Vivet *et al.* reported a 3D imaging study of the Ni-YSZ anode by using the focused ion beam SEM (FIB-SEM) tomography. They reconstructed the 3D microstructure from FIB-SEM data to visualize the interfacial features such as the surface area and TPB length, and figured out that the optimized NiO composition in Ni-YSZ would result in the largest interfacial surface area and TPB length.[81] Although FIB-SEM provides direct images of the SSGI, most measurements are destructive, and thus hard for *in situ* experiments. Other non-destructive methods such as synchrotron X-ray tomography were then used to characterize the TPB segmentation,[76] providing direct evidence of the changes of the TPB and correlated that with the fuel cell performance.

It is noted that a TPB does not only refer to the electrode–electrolyte–gas interface, but also the electrode–electrode–gas interfaces. In SOFCs, there is a long-time debate about the origin of the superior ORR activity at the heterostructured cathode–cathode–gas TPB interface such as $(La_{1-y}Sr_y)_2CoO_{4+\delta}$/$La_{1-x}Sr_xCoO_{3-\delta}$ (LSC_{214}/LSC_{113}) where either oxygen atoms or oxygen ions react and further diffuse to the electrolyte, exhibiting several orders of magnitude higher surface oxygen exchange coefficients than those at the pure thin film (*e.g.*, $La_{1-x}Sr_xCoO_{3-\delta}$) or a bulk powder cathode–gas DPB. It is hypothesized that the interfacial composition and structure affect the ORR activity. By creating a cross-section of such heterostructured thin films, Yan *et al.* used scanning tunnelling microscopy/spectroscopy (STM/STS) to study the electronic structure of the TPB under elevated temperatures.[82] They found that LSC_{214} was electronically activated at 200–300 °C and attributed this activation to the strongly anisotropic oxygen incorporation kinetics at the TPB which leads to higher ORR activity. However, the cross-section of the heterostructure with a slope cut may not represent the true TPB. To probe the interfacial structure, advanced techniques with good penetrating power are needed. Synchrotron X-ray with energy higher than 5 keV (hard X-ray) is suitable to study the buried interfaces. Feng *et al.* used surface X-ray scattering (SXRD) together with coherent Bragg rod analysis (COBRA) to examine and compare the $La_{1-x}Sr_xCoO_{3-\delta}$ cathode–gas DPB and the $(La_{1-y}Sr_y)_2CoO_{4+\delta}$/$La_{1-x}Sr_xCoO_{3-\delta}$ heterostructure TPB.[67,83] They found in both cases that there is significant Sr enrichment at the DPB surface and TPB interface (Fig. 4a), which leads to high oxygen vacancy concentration due to charge neutrality. Such oxygen deficiency is beneficial for the ORR as oxygen vacancies can not only facilitate the oxygen absorption and diffusion (Fig. 4b), but also elevate the oxygen p-band center, which is treated as the design parameter to guide the discovery of highly active cathodes and electrocatalysts for numerous electrochemical reactions (Fig. 4c).[84–87] Following Feng's research, Chen *et al.* applied a combination of synchrotron X-ray spectroscopy (*i.e.*, hard X-ray photoelectron spectroscopy) with high resolution XRD (HRXRD) to study various heterostructure TPBs and arrived at a similar conclusion that the oxygen defect chemistry of these transition metal oxides was strongly impacted by the presence of interfaces and the properties of the adjacent phases.[88]

 This journal is © The Royal Society of Chemistry 2021

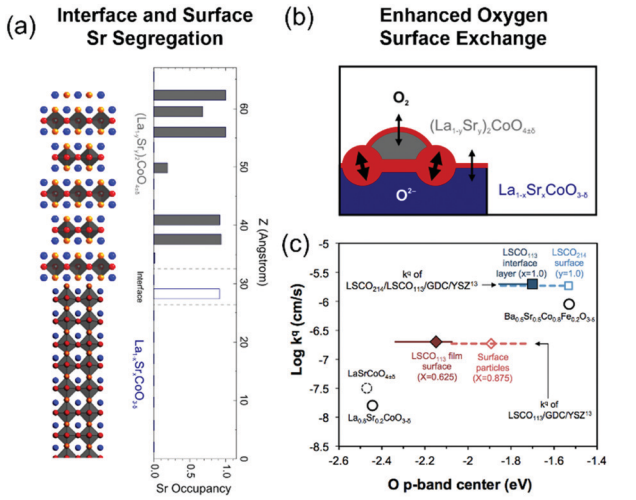

Fig. 4 (a) Model $(La_{1-y}Sr_y)_2CoO_{4+\delta}/La_{1-x}Sr_xCoO_{3-\delta}$ heterostructure thin film interfaces and layer-by-layer Sr distribution obtained from SXRD and COBRA analysis. (b) The interface and surface Sr segregation in the lattice leads to the enhanced oxygen surface exchange rate at the SSGI (c) surface exchange coefficients k^q or k^* *vs.* the calculated O 2p band centers (relative to the Fermi level) calculated for bulk unit cells. Details can be found in ref. 67.

Solid–Liquid interface

A solid–liquid interface (SLI) is another important component in many electrochemical energy systems, particularly, for electrocatalysts in energy conversion devices and electrode–electrolyte interfaces in liquid electrolyte-based batteries. Similar to a SGI, there are various interfacial processes occurring at a SLI, including electrodeposition, reactions, transformations and restructuring. The liquid medium allows the transportation of both gases and ions, adding additional complexity compared to the SGI. In addition, the SLI maintains good flexibility to adapt to structural deformation during different interfacial processes. Therefore, the complicated but important SLI attracts great scientific attention from the electrochemistry community to study the structure–property relationship in electrochemical energy devices.

Charge transfer is one major process at the SLI and is commonly found in reactions involving electrocatalysts, which typically leads to the chemical adsorption/desorption of molecules on the surface and/or the subsequent surface reconstruction. In the past few decades, efforts have been made to understand the molecular interactions with electrocatalysts and related influences on the catalytic properties.[25,89–93] The d-band center theory proposed by Norskov has paved the foundation in catalysis for linking the adsorptive power of catalysts to their activity.[94] For example, they used density functional theory (DFT) to figure out that the stable adsorbed oxygen and hydroxyl due to proton/electron transfer at the interface of the solid electrocatalysts and liquid electrolytes are the origins of the overpotential of the ORR.[95] Such studies provide guidance for rational modification of catalysts to achieve the desired activity and selectivity. Based on this theory, a lot of follow-up studies have been performed for numerous electrochemical reactions. Duan *et al.* applied DFT to predict that the transition metal modified Pt surface would have weakened the adsorption strength of hydroxyl/oxygen and then can improve the ORR performance.[96] By alloying with transition metals, Greely *et al.* tuned the adsorptive power of Pt to be optimum and successfully suggested the Pt_3Ni electrocatalyst that is cheaper than Pt but shows higher ORR activity.[97] With this theoretical guidance,[98] scientists have designed special nanostructures (*e.g.*, Pt_3Ni nanoframes) with superior ORR activity and stability (*i.e.*, no decay for more than 10 000 cycles).

In addition to theoretical studies, surface adsorption/desorption concurring with charge-transfer has been found experimentally in many cases. Due to the complexity of the interfacial changes at the SLI, thin film or single crystal model systems are usually used to provide well-defined, singly orientated surfaces. Taking RuO_2 as an example, it is a well-known, highly active electrocatalyst for the OER but its surface changes due to the interactions with molecules and reaction intermediates are largely unknown. Shao-Horn's group combined *in situ* surface-sensitive X-ray scattering techniques with DFT to study the (110)-orientated RuO_2 single crystal surface at the SLI under acidic conditions as a function of applied voltage.[99] The X-ray scattering measurements showed that (01*L*) and (10*L*) rods are the oxygen atom sensitive rods corresponding to the changes in the surface adsorbed oxygen species, and (00*L*) rods are predominantly dependent on the Ru atom position (Fig. 5).[99] When increasing the potential, the intensity of the (00*L*) rods did not change, which indicates that the position of surface Ru did not move in the OER (Fig. 5c).[99] However, the scattering intensity variation from (01*L*) and (10*L*) rods suggests the interfacial structural changes due to the adsorbed oxygen species with the applied potential (Fig. 5a and b).[99] The surface structure obtained from the fitting of X-ray scattering data provides the quantitative information of the Ru–O bonding lengths (Fig. 5d-5k).[99] With further help from DFT to examine the energetics of the surface structure, they demonstrated that the deprotonation of the hydroxyl group would form a stabilize –OO group to limit the whole OER kinetics.[99] Later, the same group carried out a more comprehensive investigation of the oxygen/hydroxyl adsorption/desorption on the RuO_2 surface with four different orientations, namely (101), (110), (001), and (100), using a combination of AP-XPS, *in situ* SXRD, and DFT.[100] They found that different surface orientations can have different degrees of influence on the adsorptive powers for reaction intermediates and can be used to tune the OER activity of the catalysts by varying the density of active sites.[100] These two cases are from few experimental studies that directly reveal the molecular adsorption/desorption is caused by charge-transfer in reactions,[98,101,102] mainly due to the minor or negligible local structural changes at the SLI from molecule adsorption/desorption. It is more plausible to monitor the electronic structure changes at the SLI using spectroscopy, as charge-transfer can modify the electron configurations.[103–105]

Strong interfacial restructuring can also be induced by the charge-transfer process at the SLI and is also common in

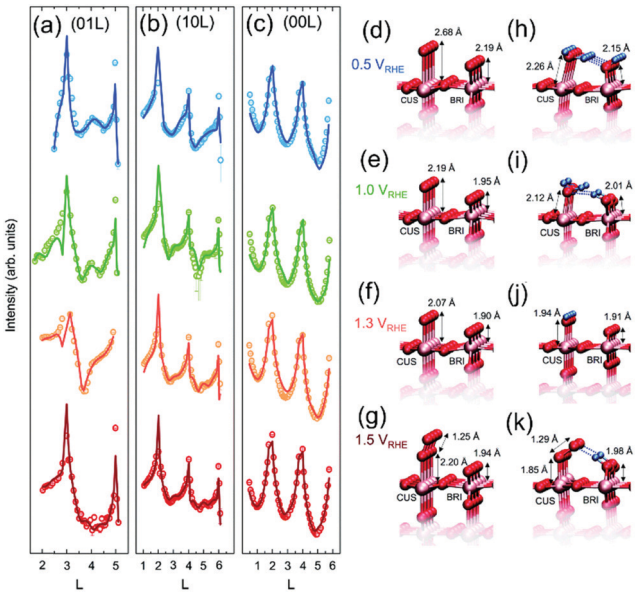

Fig. 5 (a) (01*L*) (b) (10*L*) and (c) (00*L*) rods measured at the four different potentials, 0.5 V, 1.0 V, 1.3 V and 1.5 V as indicated. All voltages here are *versus* the reversible hydrogen electrode (RHE). The experimentally measured intensities are shown as open points and the best-fit results from the fitting process are shown as solid lines of the corresponding color. Ball and stick models for the best-fit structures obtained for the (d) 0.5 V, (e) 1.0 V, (f) 1.3 V and (g) 1.5 V crystal truncation rod data. Maximum experimental uncertainty in bond lengths is 0.06 Å. The most stable adsorbate configuration obtained from DFT calculations at (h) 0.5 V and (i) 1.0 V. The Ru_{CUS}–O bond length is the average value of the Ru_{CUS}–H_2O (2.17 Å) and Ru_{CUS}–OH (2.07) Å and the Ru_{BRI}–O bond length is an average value of the Ru_{BRI}–OH (2.10 Å) and Ru_{BRI}–O (1.92 Å) at (j) 1.3 V and (k) 1.5 V. The Ru_{CUS}–O bond length is the average value of the Ru_{CUS}–O (1.73 Å) and Ru_{CUS}–OO (1.96) Å and the Ru_{BRI}–O bond length is an average value of the Ru_{BRI}–OH (2.07 Å) and RuBRI–O (1.89 Å). Pink, red and blue spheres represent the Ru, O and H atoms respectively. Bond lengths between surface Ru and adsorbed O species are labeled. (Ru_{CUS}: a coordinately unsaturated Ru site bound to five O atoms; Ru_{BRI}: a bridge Ru site bound to six O atoms).[99]

electrocatalysis.[106–111] The restructuring can be either reversible or irreversible. The former is generally good for the long-term use of electrocatalysts and has been reported in many studies,[110,112–118] while the latter is believed to be detrimental to the performance of catalysts. In most cases, the surface of the electrocatalysts becomes amorphous and they lose their original activity. Experiments have demonstrated that perovskite $Ba_{0.5}Sr_{0.5}Co_{0.8}Fe_{0.2}O_{3-\delta}$ (BSCF82) is not only highly active as the cathode in SOFCs to promote reactions at the SGI, but also a good electrocatalyst for the OER in alkaline solutions. However, it is not stable during the reaction.[119] To study the deactivation mechanism, May *et al.* applied high resolution transmission electron microscopy (HRTEM) to compare the surface of the BSCF82 before and after the reaction. They found that the surface amorphization caused by the reduced surface concentration of Ba and Sr ions in the charge-transfer catalytic process is the reason for the degradation of the OER activities.[120] However, not all amorphization leads to the activity loss for electrocatalysts. $SrIrO_3$, a recently discovered material with ~3 orders of magnitude higher in OER activity compared to the commercial standard IrO_2 under acidic conditions, exhibits better performance during cycling.[121] This was originally attributed to the Sr leaching and the formation of the IrO_2/$SrIrO_3$ heterostructure. The follow-up mechanistic study, which combined surface-sensitive scattering as well as spectroscopy and DFT, reveals that there are actually two changes of $SrIrO_3$ during the reaction.[122] The Sr leaching results in the Sr-deficient Sr_yIrO_x, and at the same time the top surface (~2.4 nm) turns into an amorphous structure. This special interfacial restructuring is initiated by the lattice oxygen redox and is beneficial for the OER due to the coupled ionic diffusion.[122] Instead of forming a special heterostructure, the highly disordered Ir octahedral network with Ir square-planar motifs in the amorphous layer is confirmed by DFT to be the active center of the electrocatalyst.[122]

We want to emphasize that the irreversible restructuring at the SLI other than amorphization could also be good for electrocatalysts at the SLI. Several studies have shown that there could be an activation change in electrocatalysts at the very beginning of the reaction. In a study of single Ru atom anchored on the transition metal double layer hydroxide as the electrocatalyst for the OER, Li *et al.* identified Ru–O–M (Fe, Co, Ni, and Cu) motifs on the electrocatalyst surface after synthesis and detected the shortening of the bond length after the first cycle. They suggest that the Ru–O–M configuration changes the electron distribution and promotes the electron transfer from M to Ru.[123] These electron transfers would not only benefit the oxygen adsorption confirmed by DFT but also prevent the Ru from being oxidized to a higher oxidization state and dissolving in the electrode, consequently increasing the electrochemical stability.[123] A similar situation was found in another study using nickel–iron layered double hydroxide as the OER electrocatalyst. Interestingly, the Ni goes through reversible oxidation state changes in the reaction while Fe experiences irreversible restructuring initially. The reversible change of Ni contributes to the regulation of the local structure and makes high-valent metal sites stable at low overpotentials.[124] The irreversible change of Fe enables a special Fe^{4+} state that serves as the active site for the OER and contributes to high activity of the layered double hydroxide.[124]

All these examples shown above suggest that interfacial restructuring is a complicate process at the SLI. To better track such changes with deep understanding, *in situ* and *operando* characterization methods such as X-ray absorption spectroscopy (XAS) are necessary.[123,125–127] One good example is from our study on high-loading atomically dispersed Ir atoms anchored on the amorphous CoO surface using *in situ* XAS.[125] Although XAS is a bulk-sensitive technique, the material of interest is on the surface so the measurements on the material become surface-sensitive. As shown in Fig. 6a, the X-ray absorption near edge structure (XANES) pointed out that Ir would be oxidized with the increasing applied potential and reduced with the decreased applied potential.[125] Extended X-ray absorption fine structure (EXAFS) indicated that the surface anchored Ir would move towards the CoO bulk to form a strong Ir–O–Co bond (Fig. 6b). In addition, EXAFS also shows the increase and

 This journal is © The Royal Society of Chemistry 2021

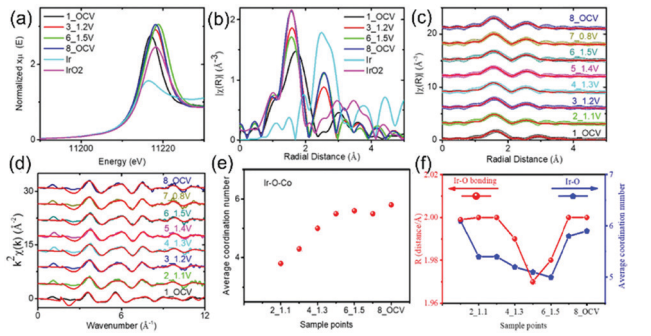

Fig. 6 XAS results of $Ir_1Co_{13.3}O_{20.1}$. *In situ* Ir L-edge (a) XANES and (b) EXAFS under various reaction potentials. Fourier transfer EXAFS fitting of *in situ* Ir during the reaction: (c) *R*-space and (d) *k*-space. The average coordination number of Ir–O–Co during the OER (e). The Ir–O bonding distance and the average coordination number of Ir–O during the OER (f).[125]

decrease of the Ir–O coordination number (Fig. 6c–e), which stands for the oxygen species adsorption and desorption, respectively.[125] Such reversible restructuring of Ir–O–Co bonding, as discussed above, would change the electron distribution around Ir and Co, thus benefiting the oxygen adsorption/desorption during the charge-transfer process at the SLI.[125] Furthermore, a lot of bulk-sensitive techniques can be tuned surface-sensitive when operating at a grazing-incidence angle.[128,129] For example, Lee *et al.* carried out the *in situ* grazing incidence XAS (GIXAS) and XRD (GIXRD) to study the polycrystalline Cu thin film surface during the electrochemical carbon dioxide reduction reaction (CO2RR).[129] Their results showed that the surface CuO would be reduced to Cu that is the only phase presenting under the CO2RR conditions, and the polycrystalline Cu surface would be reconstructed towards the Cu (100) surface.[129] This is similar to our study on the reconstruction of copper(II) phthalocyanine (CuPc) during the CO2RR.[118] We also found the reduction of CuPc to form Cu nanoclusters, but differently our results indicate that these Cu nanoclusters can be reversed back to CuPc once the applied potential is back to the open circle potential, thus CuPc can be reused many times in the reaction.[118] Similar processes observed by the two groups with different final products in the CO2RR are not contradictive to each other. The difference could be due to the nucleation and growth conditions. In the CuPc case, the size of Cu nanoparticles is too small to have a stable nucleation seed and then decomposes once the potential is reversed, while the Cu thin film could be strongly bonded by the underneath substrate without further change. These two studies also emphasize the importance of advanced *in situ* characterization techniques for investigating complex interfacial processes at the SLI.

Besides the electrocatalysts and/or electrode influence on the SLI, we also want to bring attention to the electrolyte influence at the SLI.[130–136] The pH of the electrolyte is one important parameter affecting the molecular absorption capability at the SLI.[131,133] Li *et al.*, used IrO_x as a model system to demonstrate that IrO_x shows 6.5 times higher OER activity in 4.0 M KOH than 0.1 M KOH due to the stronger OH^- adsorption.[132] They further pointed out the adsorption and interaction OH^- would also be affected by using different cations at the same pH.[132] They found that the Na^+ would help in forming a stronger noncovalent interaction with OH than K^+ to decrease the interfacial OH^- mobility, which worsens the OER performance.[132] In addition, Waegele *et al.* recently reviewed that the electrolyte cation can change the electric double layer, reaction rates, and selectivity a lot by influencing the SLI.[136] Moreover, the anion would also affect the surface absorption and restructuring at the SLI.[130,133] Arminio-Ravelo *et al.* studied the SLI by using standard Ir-based nanoparticles in two different acid electrolytes (H_2SO_4 and $HClO_4$). They found that Ir black nanoparticles are likely to be oxidized faster in H_2SO_4 than in $HClO_4$ which causes Ir to be less active in H_2SO_4 than $HClO_4$.[133]

When moving from electrocatalysts to the electrode–electrolyte SLI in liquid–electrolyte-based batteries (LEBs, such as lithium/sodium ion batteries, aqueous batteries, multivalent batteries, and dual-ion batteries), the interfacial processes become more complicated.[137–146] For electrocatalysts, although charge-transfer induced changes such as molecule adsorption/desorption dominate at the SLI, there is little or no reaction between the electrocatalyst and the electrolyte.[19,29,147] However, since both ion and electron transfers take place at the SLI in the LEBs, electrodeposition and interfacial transformation could also be induced in addition to interfacial restructuring discussed in electrocatalyst systems.[93,148,149] For example, the well-known SEI in lithium–ion batteries is a product from these complex interfacial processes, which involve the decomposition of the electrolyte, electrodeposition of the reaction products on lithium metal or graphite anodes, and interfacial restructuring at the anode side.[150] Studies on SEIs have been carried out for a long time but limited progress has been achieved due to the difficulties in detecting the dynamic formation of thin interfacial layers that contain mostly light elements. Until recent years, with the application of advanced cryo-electron microscopy and synchrotron X-ray scattering,[11,151–154] researchers can study the SEI, either quasi-*in situ* at the frozen state or completely *in situ* and obtain the structural and compositional information at the atomic-scale. These studies have shown that the SEI is composed of both crystalline and amorphous structures and contains not only LiF but also LiH. In addition to lithium-ion batteries, the SEI is also an important component in other LEBs.[25,155–157] Ko *et al.* reported a SEI formed at the anion-derived solid electrode and liquid electrolyte interface, which would decompose or dissolve in the free (or uncoordinated) water molecules but can be retained stably in the water-in-salt electrolyte.[92] This SEI is critical as it can expand the operating voltage window in aqueous batteries and suppress the side hydrogen evolution reaction.[92] Furthermore, Munster *et al.* found a SEI consisting of the degradation products of bis(fluorosulfonylimide) (FSI) salt at high concentrations in potassium dual-ion batteries.[148] The SEI formation would suppress the degradation of the solvent during potassium (de)intercalation and reduce the charge transfer resistance.[148]

Comparatively the cathode–electrolyte interphase (CEI) is easier to study. The CEI is formed on the oxide (*e.g.*, $LiCoO_2$) surfaces which can be studied not only on powders using advanced techniques such as cryo-electron microscopy but also on thin film model systems with well-defined surfaces.[158] Lu *et al.* grew $LiCoO_2$ (LCO) microcrystals on Al substrates and used *in situ* atomic force microscopy (AFM) to investigate the surface morphology. They found that the LCO would react with the liquid electrolyte ($LiPF_6$) and Co will continue dissolving into the electrolyte at higher voltages above 4.2 V.[150] They also found that when adding a thin Al_2O_3 layer on top of LCO, the reaction between $LiCoO_2$ and $LiPF_6$ can be suppressed.[150] Interestingly Al_2O_3 is neither Li^+ conducting nor electron conducting. Therefore, a lot of efforts have been focused on understanding how such material can be beneficial for interfacial progress.[9,10,159–161] Particularly, our group developed a facile synthesis protocol *via* the sol–gel method to coat Al_2O_3 on a commercial LCO surface and investigated the thickness-dependent effects on the battery performance.[62] It turned out that a very thin layer (50 nm or less) has good mechanical flexibility and does not block Li^+ diffusion at the SLI. By employing XAS, we showed that unprotected or incompletely covered LCO would react with the Li ions to form Li_2O and reduce LCO to Co, thus causing the degradation of both the electrode and electrolyte.[62] In contrast, a thick Al_2O_3 coating would affect the ionic and electronic conductivity, which increases the transportation resistance and decreases the overall battery performance.[62] This surface coating strategy has been successfully applied on cathodes and anodes in batteries to prevent unwanted interfacial reactions at the SLI, and can be extended to other electrode–electrolyte interfaces to improve the interfacial stability.

Besides the formation of an interphase at the SLI, ionic diffusion across the interface is another important interfacial process in LEBs. The host structure at the electrode can strongly influence the ionic diffusion at the SLI, as demonstrated by the $LiMn_2O_4$ (LMO) cathode that can take up two Li^+ at the maximum but in a commercial battery cell, it is only cycled with one Li^+ to maintain the structural stability.[162] To figure out ways for improving the energy capacity of LMO, Chen *et al.* used thin films to obtain epitaxially grown LMO. The lattice confined structure enables the capability of LMO to host two Li^+ without any phase transition, which is confirmed by *in situ* and *operando* X-ray reflectivity and XRD during Li insertion and extraction.[162] They further found that no measurable Mn dissolution/loss during the Li insertion but dramatic Mn loss during the deeper discharge causing by the lattice strain change of LMO, which provides new insights into how to improve the capacity while maintaining the stability of LMO.[162] The strategy of using lattice confinement has been applied in multivalent batteries as well. The MgO substrate to induce strain, high-temperature high-pressure phase of cubic $MgMn_2O_4$ (MMO) has been synthesized at room temperature as the thin film electrode.[163,164] Different from powder MMO with the tetragonal structure that is hard to intercalate Mg^{2+}, the cubic MMO thin film can be reversibly inserted/extracted

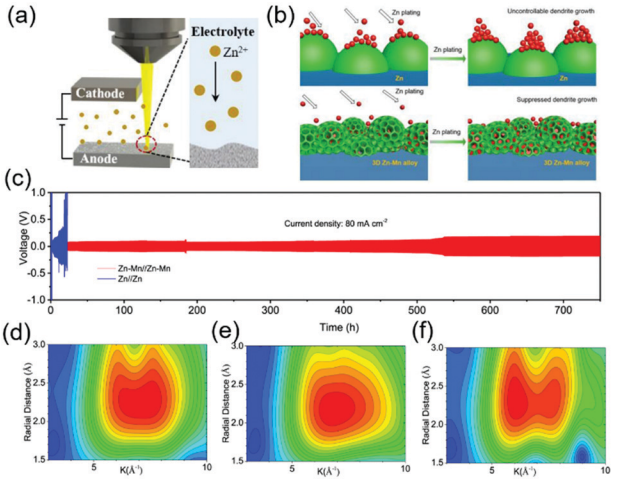

Fig. 7 (a) Schematic illustration of the *in situ* optical visualization experimental setup. (b) Schematic illustration of Zn plating processes on the Zn anode (top) and Zn–Mn anode (bottom). (c) Long-term galvanostatic cycling performance of symmetric Zn–Mn and pristine Zn cells at a current density of 80 mA cm^{-2} (areal capacity: 16 mA h cm^{-2}; electrolyte: 2 M $ZnSO_4$ in seawater). Wavelet transform of Mn K-edge EXAFS for the (d) pristine Zn–Mn anode, (e) fully discharged Zn–Mn anode, and (f) fully charged Zn–Mn anode.[2]

with Mg^{2+},[4,165] which can be attributed to the improved ionic diffusion in the bulk and also at the SLI compared to the MMO polymorph. Another consequence of the ionic diffusion at the interface is the result of electrodeposition, or so-called dendrite formation at the metal anode. It has been shown that the dendrite can short the battery and cause safety issues. However, to increase the energy density (*e.g.*, towards 500 kW kg^{-1}) of batteries the use of metals as anodes is necessary. The control of the dendrite formation at the metal anode and the inhibition of unwanted ionic diffusion at the SLI thus become challenging problems.[1] Numerous methods have been proposed to suppress, regulate and eliminate the dendrites in LEBs.[166–170] In particular, our group, in collaboration with the Yang group at the University of Central Florida, developed ZnMn alloys (Fig. 7a) that can achieve consistently superior performance at a high current density (80 mA cm^{-2}) over thousands of cycles (Fig. 7b) under harsh electrochemical conditions, including testing in seawater-based aqueous electrolytes as the anode in multivalent aqueous batteries.[2] The alloy anode is synthesized by an electrodeposition method that involved initiating the growth on the electrode surface leading to clusters of alloy deposits which then combine to form a 3D structure. The *in situ* optical visualization (Fig. 7a) coupled with finite element analysis confirmed that such a structure at the SLI allows Zn to deposit easily inside the nano-voids, thus avoiding the dendrite formation. These voids also allow other cations such as Mg^{2+} and Na^+ in the seawater to adsorb.[2] Furthermore, the Zn ions would have a much faster deposition rate in the trench than that at the protruding region, which also minimized the dendrite formation (Fig. 7).[2] With the help of XAS imaging (Fig. 7c–e), the reversible changes of the anode in the charged

 This journal is © The Royal Society of Chemistry 2021

and discharged states have been confirmed, suggesting the effectiveness of the strategy to inhibit the unwanted dendrite deposition at the SLI. This concept, although demonstrated in aqueous batteries, can result in a paradigm shift in the design of high-performance alloy anodes for both aqueous and non-aqueous batteries which will revolutionise the battery industry.

As seen in the discussion above, the interfacial processes at the SLI are much more complicated than at the SGI. However, not all of them lead to damage to electrochemical energy devices. By understanding the formation and evolution of interfaces in reactions, one can come up with suitable strategies to promote the positive and/or inhibit the negative interfacial processes with improved performance of the whole system.

Liquid–gas interface

A liquid–gas interface (LGI) is important but sometimes is ignored in many electrochemical energy devices involving gas reactants and liquid electrolytes, such as the ORR and OER in metal–air batteries, ORR and hydrogen evolution reaction (HER) in fuel batteries, and CO2RR, and nitrogen reduction reaction (NRR).[171–174] For these systems, the dissolution and diffusion of gas reactants and subsequent reaction intermediates in liquid electrolytes can affect the overall reaction rates by changing the concentration of reactants transferring to the electrocatalysts and electrodes based on the chemical reaction rate law.[175,176] For example, the higher concentration of the alkaline electrolyte (*e.g.*, 1 M of KOH) can provide more OH^- ions that facilitate the transportation and formation of reaction intermediates (OH*) in the ORR.[177–179] The mass transfer of gas reactants also depends on the diffusion rate and concentration that are related to the solubility of the gas. The quantitative study of the mass transfer in electrochemistry can be obtained using the Levich equation, where the Levich reaction current (or the limited current) depends on the diffusion coefficients, kinematic viscosity, angular rotation rate, and gas concentration. The dissolution directly affects the gas concentration.[180,181] Some studies suggest using ionic electrolytes to improve the solubility of the gas in the electrolyte and then to increase the reaction rate.[134,182–184] For example, Gittleson *et al.* systemically studied the oxygen transport in the electrolyte with both experimental and computational techniques.[184] Their results indicate that electrolyte salts would affect the oxygen solubility (*i.e.* large anions such as $TFSI^-$ and $BETI^-$increase oxygen solubility compared with smaller anions such as BF_4^-), and the solvents of the electrolyte have an influence on the oxygen diffusivity. Besides the gas concentration, all the three left parameters (diffusion coefficients, kinematic viscosity, and angular rotation rate) influence the diffusion rate. For most inorganic electrolytes such as 1 M KOH solutions, 1 M $KHCO_3$ solutions, and 1 M H_2SO_4 solutions used in energy devices mentioned above, the solubility of gases (*e.g.*, O_2, CO_2, and H_2) in these electrolytes is low, and the diffusion coefficient and kinematic viscosity are constant. One way to improve the mass transfer is to increase the flow rate of the liquid containing the dissolved gas reactants to the electrodes. In rotating disk electrode experiments, this can be achieved by changing the electrode rotation speeds, and in practical fuel cell and metal–air devices, the flow electrolyte cell design can help.[185–188] Since the diffusion coefficient and kinematic viscosity are physical constants determined by the electrolyte itself, not many studies in electrocatalysis focus on them since the change of the electrolyte may also induce the change of electrolyte/electrode interfaces, thus making the system more complicated.

Solid–solid interface

A solid–solid interface (SSI) is commonly found in many thin film devices such as semiconductor electronics. The epitaxial growth of oxides leads to a heterostructured SSI that can be used as a model system to study electrochemical reactions such as batteries and catalysts.[86,163,164,189–193] In the SGI portion of this Feature Article, we have discussed a special solid–solid triple-phase boundary that involves ionic diffusion, charge transfer and restructuring at the electrolyte–cathode–gas interface. Here we will mainly focus on the SSI in energy storage systems, particularly solid-state batteries (SSBs),[194–198] which use non-flammable solid-state electrolytes (SSEs) instead of flammable liquid state electrolytes (LSEs). The advantages of using SSBs lie in not only their better safety than commercial LIBs, but also their compatibility with the lithium metal anode to suppress the dendrite formation and gain high energy density.[3,199–201] Hence, SSBs are one of the most promising next-generation energy storage systems to replace LIBs and have attracted a significant amount of attention from both academia and industry.[3,199–205] Since repeated operations are needed to run SSBs, a high mechanical modulus and chemical stability for each component are required, and in particular, for the SSIs that connect two dissimilar materials. However, maintaining high stability at SSIs is challenging due to the inevitable restructuring and possible side reactions at these interfaces. Some investigations have also found that SSBs still suffer from lithium dendrite formation, which causes an electric short and in turn shortens the cycle life of batteries.[206,207] The improvement of the interfacial properties at the SSI becomes one of the most urgent tasks in the battery community. Like the SEI in the SLI in LIBs, the formation of an interphase layer at the solid electrode–electrolyte interface has recently been treated as a successful strategy to suppress the formation of dendrites and maintain SSI stability. Zhang *et al.* reported that the *in situ* formed nanoscale interface layer between novel poly(vinylidene difluoride) (PVDF)-based solid electrolytes and the Li anode leads to an open-circuiting feature instead of short-circuiting at high current density and avoids the risk of over-current, which can suppress the Li dendrite growth.[208] Besides the *in situ* self-formed SSI layer, Hou *et al.* demonstrated that a LiF- and Li_3N-enriched artificial SSI constructed by an *ex situ* electroplating method[209] could stabilize the metallic Li anode and improve

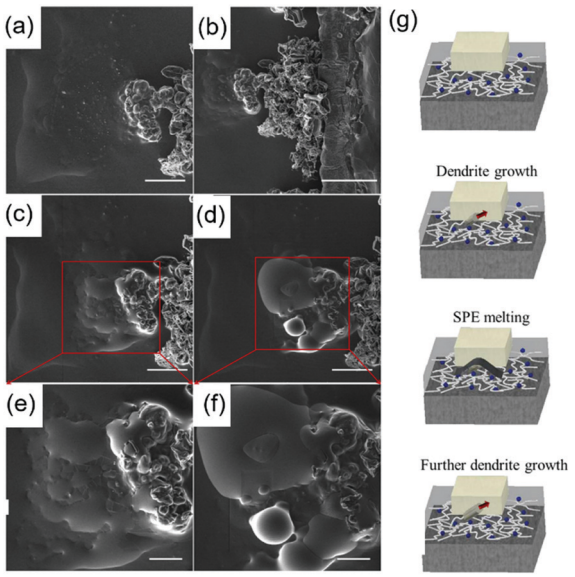

Fig. 8 SEM images of the polymer and (g) schematic showing dendrite growth. SEM images. (a) After 3 days of cycling (scale bar representing 50 μm), (b) after 7 days of cycling (scale bar representing 100 μm), (c) after 9 days of cycling (scale bar representing 50 μm), and (d) after 13 days of cycling (scale bar representing 50 μm). (e) High magnification of the red box in image (c) (scale bar representing 20 μm), and (f) high magnification of the red box in image (d) showing the morphological change on the SPE (scale bar representing 20 μm). (g) Schematic of the dendrite formation and the effect of SPE melting on further dendrite growth.[210]

the interface compatibility at the Li anode side to suppress the dendrite formation.[209]

Numerous studies have shown ways to modify and improve the chemical and mechanical properties of the SSI. However, relying on trial-and-error methods to design a stable SSI is not trivial and rational. It is essential to first understand the interfacial processes at the SSI including the formation of Li dendrites, the reactions and charge-transfer induced transformations. For example, to study the Li dendrite formation at the anode surface during cycling (Fig. 8), Golozar *et al.* used the *in situ* SEM combined with energy-dispersive spectroscopy (EDS),[210] and observed an apparent morphological change in the solid polymer electrolyte (SPE) when cycling the battery, which was believed to be the decomposition and degassing of the polymer electrolyte (Fig. 8).[210] When increasing the cycling time, the dendrites were formed in the polymer regions causing further decomposition of the electrolyte at the SSI, or some reactions between Li and the electrolyte (Fig. 8).[210] They pointed out that the morphological change on the electrolyte caused by Li or decomposition interactions would be the problem for further Li dendrite growth and then the failure of the battery.[210] Moreover, Wang *et al.* applied time-resolved EIS and ultrasensitive 3D chemical analysis from time-of-flight secondary-ion mass spectrometry (ToF-SIMS) to study the intricate SSI and directly visualize the dendrite structures.[211] The results indicated that the electrolytes react with the metal electrodes at varying degrees upon contact, which is in contrast to the traditional options that dendrites were formed only during charging/discharging processes.[211] These formed interphases widen the electrochemical window, but their electronic and ionic conductivities determine the battery performance and have a large influence on dendrite growth.[211] Based on the experimental results, they carried out thermodynamic analysis of the interphase, and showed that an interphase with low electronic conductivity, high ionic conductivity, good chemical stability, a dynamic thickness and uniform coverage is good to prevent dendrite growth.[211] They also pointed out that a relatively stable electrolyte with a metal anode promotes fast dendrite growth. Hence, the general search for chemically stable electrolytes helps improve the performance of SSBs.[211]

In addition to the dendrite formation at the anode–electrolyte interphase (AEI), the interfacial reactions between SSI and ions (*e.g.*, Li^+) can form a passivation layer in polymer-based electrolytes or an unstable interphase in sulfide-based electrolytes, thus affecting the SSB performance. Since lithium is a highly reductive metal, it can quickly extract hydrogen from the polymers or break the polymer backbone to form Li–O–R (R: organic groups such as OCH_3) types of compounds.[212,213] Granvalet-Mancini *et al.* used atomic force microscopy (AFM) to show the formation of a passivation layer and attenuated total reflection Fourier transform infrared (FTIR) spectroscopy to detect the presence of CF_3 radicals in this passivation layer,[214] which has lower ionic conductivity and is bad for battery performance. One solution for preventing side reactions at the SSI is to either *in situ* form or *ex situ* add an artificial stable layer at the AEI.[215–218] Li *et al.* grew a Li_3PO_4 thin film layer as an artificial AEI during the Li deposition/dissolution process.[217] The Li-conducting Li_3PO_4 layer can effectively reduce the side reactions between the Li anode and polymer electrolyte.[217] Besides creating a stable AEI, Zhang *et al.* developed a superior blend solid polymer electrolyte with integrated hierarchical architectures, which exhibits high ionic conductivity and good thermal stability.[216] Due to the unique structure and composition, a stable blend polymer and Li interphase were formed at the SSI, avoiding side reactions to form a passivation layer.[216] Similarly, sulfide-based electrolytes suffer from a similar situation to polymer electrolytes. Once the Li anode encounters sulfide-based electrolytes, side reactions could occur to form the decomposition products such as Li_2S, unstable Li_3P, LiX (X = Cl, Br, I), and other compounds with remaining elements (Si, Ge, Sb, As, and Sn).[213,219–221] Zhu *et al.* performed a first-principles study to estimate the decomposition energies of different solid electrolytes and suggested that $Li_{10}GeP_2S_{12}$ (LGPS) would decompose into Li_3P_4, Li_2S, and $Li_{15}Ge_4$, and Li_3PS_4 would decompose into Li_3P and Li_2S.[194,222] Later, Wenzel *et al.* utilized *in situ* XPS to experimentally determine the compositions of the interphase during the electrochemical measurements.[223] They found that $Li_{10}GeP_2S_{12}$ decomposed to Li_3P_4, Li_2S, and some Li–Ge alloys (Fig. 9), which is in perfect agreement with the theoretical predictions.[223] Clearly, the compositions at the anode–electrolyte interphase depend on the electrolytes (*e.g.*, Li_2S from Li_3PS_4[224]) and if the interphase is evitable, it should be formed with properties close to an ideal AEI with only Li–ion

 This journal is © The Royal Society of Chemistry 2021

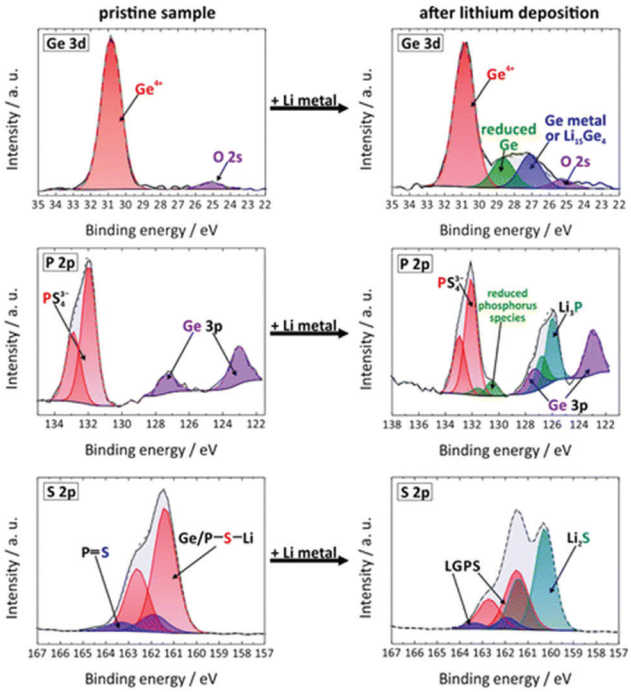

Fig. 9 S 2p, Ge 3d, and P 2p XPS spectra and model fits for the pristine LGPS sample and after deposition of the 31 nm Li metal. The identified species are marked and labelled in different colors. The small oxygen signal is caused by tiny fractions of oxygen in the atmosphere of the XPS chamber.[223]

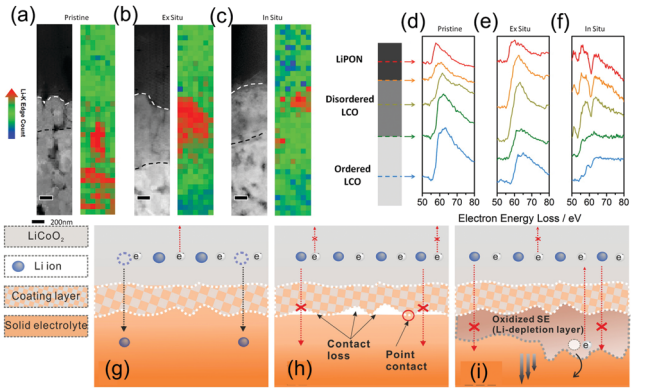

Fig. 10 STEM image and EELS characterization. (a–c) High-angle annular dark-field image of the nanobattery stack along with the Li K-edge concentration mapping of (a) pristine, (b) *ex situ*, and (c) *in situ* samples with scale bar representing 200 nm. (d–f) Li K-edge spectra from various parts of the layers are displayed for (d) pristine, (e) *ex situ*, and (f) *in situ* samples.[235] Schematic description of three possible situations occurring in a model SSBs with $LiCoO_2$ as the active material and LGPS as the solid electrode. (g) The ideal case: intimate contact between the SE and c-$LiCoO_2$, and no mutual reaction or decomposition of the SE. (h) Contact loss due to volume changes or failures during preparation. (i) Decomposition of the SE at high voltages, forming a Li^+-depletion layer, thereby inhibiting Li^+ mobility.[236]

conductivity but no electron conductivity to block further reactions at the interface.[225,226] An unstable AEI with both Li-ion and electron conductivities will cause a continuous reaction between the lithium metal and the sulfide-based electrolyte, consuming both materials and reducing the cycle life of the SSBs.[225,226] Similar work is carried out to improve the stability at the Li metal and polymer electrolyte interface.[219,227] For example. An artificial AEI layer that only conducts Li-ions with high compatibility to Li metal can be introduced to improve the interface stability.[227,228] Simon *et al.* came up with a stable solid polymer electrolyte as a protection layer between the Li anode and Li_6PS_5Cl electrolyte. The XPS results confirmed that the polymer would form a durable interphase layer with Li_6PS_5Cl, consisting of polysulfides and LiF. The low resistance and easily formed layer protected Li_6PS_5Cl from decomposition.[229] One has to be cautious that the interfacial reaction and dendrite growth can take place at the same time. Once the Li anode reacted with the electrolytes or grew into Li dendrite, it may recede a few microns, causing a worse connection between the anode and electrolyte. Therefore, strong adhesion or surface modification between the Li anode and electrolyte is a standard solution to ensure a good connection.[213]

Another SSI in SSBs is the cathode–electrolyte interface, which has less issues for Li dendrite formation. However, there are also ionic diffusion and charge transfer at such an interface to form a CEI. Similar to the AEI, the cathode and electrolyte interfaces are mechanically rigid and can become unstable with an interphase layer during battery charging/discharging processes.[230–232] An interphase is predicted by the theoretical calculation and confirmed by XPS to form at the $LiCoO_2$/LiPON interface.[194,233,234] Later, Wang *et al.* conducted *in situ* scanning transmission electron microscopy (STEM) coupled with electron energy loss spectroscopy (EELS) and revealed a disordered interfacial layer between $LiCoO_2$ and LiPON that accumulates Li and evolves to rocksalt CoO after cycling (Fig. 10a–f).[235] This CEI could be caused by the cathode reacting with the highly delithiated LiPON.[235] The increasing thickness of this layer would lead to a rapid capacity decay as more of the cathode will be rendered electrochemically inactive.[235] Generally, a CEI that allows both electron and ion transfers is very unstable and can cause continuous reactions of the electrolyte and the cathode.[194,232] Zhang *et al.* also found that the $LiCoO_2$/$Li_{10}GeP_2S_{12}$ interface was quite unstable and degraded during battery operation.[236] They used XRD to show the decrease of the grain size of the cycled $LiCoO_2$, which worsens the connection between the cathode and electrolyte (Fig. 10g–i).[236] Their EIS and XPS results suggested that the decomposition products are a mixed electronic and ionic conductors, which allows for further oxidization of the electrolyte (Fig. 10g–i).[236] In some cases, the CEI could conduct both Li and other ions, and subsequently leads to additional side reactions. Groh *et al.* demonstrated that Fe ions can diffuse through the $LiFeO_4$/$Li_{3+x}P_{1-x}Si_xO_4$ layer and react with the $Li_{3+x}P_{1-x}Si_xO_4$ electrolyte,[237] which produces $LiFePO_4$–Fe_2SiO_4 and Li_3PO_4–Li_2FeSiO_4, causing capacity fading.[237] While in other cases, CEIs are just passivation layers with high resistance due to bad ionic and electronic conductivity.[230–232,238,239] As demonstrated by Kim *et al.* that $Li_7La_3Zr_2O_{12}$ would react with the $LiCoO_2$ to form an interphase layer (around 50 nm

thickness).[240] TOF-SIMS confirmed that the interphase consists of Al, Zr, La, and Co, affecting the initial Coulombic efficiency and cycle life.[240] To solve the instability of the CEI or prevent side reactions at the interface, a similar strategy to that used for the AEI was applied by introducing an artificial SSI or a protecting layer on the cathode.[213,241] For instance, the polyacrylonitrile (PAN)-based gel can soften and wet the cathode–electrolyte interface to reduce the internal resistance of the whole battery.[242] $Li_2CoTi_3O_8$ was designed as an artificial SSI between $LiCoO_2$/$Li_{10}GeP_2S_{12}$ with high interfacial affinity due to thermodynamic and electrochemical compatibility with both the cathode and electrolyte, thus enabling excellent cyclability for the SSBs.[243]

In the examples shown above, various interfacial processes take place at the SSI, which can lead to all kinds of interphases with different compositions and morphologies. It is essential to understand these processes, particularly during battery operation, and establish the structure–property relationship to guide battery design. Advanced characterization methods are necessary for *in situ* studies. In addition to lab-based tools such as XPS, TEM, EELS, and ToF-SIMS, synchrotron X-ray scattering, spectroscopy and imaging techniques bring unique capabilities for studying the buried solid–solid interfaces to provide information related to the atomic as well as electronic structure, composition and morphology of the materials.[244,245] Insights obtained from these studies can further help in the development of stable SSIs for high performance SSBs.

Summary and perspective

The increasing demand for energy and high environmental standards of carbon neutral emission requires the development of green, sustainable energy storage and conversion devices. Electrochemical energy systems, due to their zero or negative carbon emission, have emerged as promising candidates. However, to enable large-scale applications, their performances must be further improved, which lies in the reduction of unwanted side reactions and products to achieve high efficiency and good stability. A lot of issues have been identified at interfaces which are key components in these systems as they connect the electrodes and electrolyte together. Improvement in the electrode–electrolyte interfaces can lead to the advancement of the whole systems. Therefore, we review and discuss various interfacial processes, including electron/charge transfer, ionic transfer, surface reconstruction and adsorption/desorption, at three interfaces, namely solid–gas, solid–liquid and solid–solid. Owing to their unique combinations, representative electrochemical energy systems are chosen and illustrated accordingly. The three interfaces change differently and can have either positive or negative effects on the performance of electrochemical energy devices. Hence, we should deal with the interfaces case by case. For solid–gas interfaces, the gas adsorption is the first step of all interfacial processes. The construction of beneficial interfaces (*e.g.*, DPB and TPB) must have an effective function to facilitate the adsorption, diffusion, and reaction of gas molecules. Considering the ionic and electron transfer associated with the reactions at the solid–gas interfaces, the electrodes are preferred to be the mixed ionic and electronic conductors while the electrolyte is only allowed to conduct ions. The DPB and TBP should be able to tolerate the structural and composition changes induced by gas/ion diffusion and interactions. For solid–liquid interfaces, charge-transfer and ion-transfer are two major processes that can result in various unwanted or desired interfacial changes such as adsorption/desorption of reaction intermediates, surface restructuring and deposition. In electrocatalysis, charge-transfer is related to the electronic structure at interfaces. Tuning the proper electronic structure (*e.g.*, metal d-band center and oxygen p-band center) can achieve optimal adsorptive power for reaction molecules or intermediates with less undesired surface restructuring. In liquid–electrolyte-based batteries, ion-transfer is the dominant process that can lead to interfacial restructuring and the formation of interphases, which sometimes are facilitated by the charge-transfer process and are quite complicated. Although the SEI is known to be beneficial for lithium–ion batteries, it is not always a good interphase in other batteries such as multivalent batteries. If the interfacial restructuring is inevitable, one should make sure that the formation of interphase(s) can only permit ion-transfer instead of electron-transfer at the solid–liquid interfaces in batteries and maintain the structural stability during ionic diffusion through the electrodes. For solid–solid interfaces, the major effort right now is to reduce the interfacial resistances and metal dendrite formation in solid-state batteries. Promising results have been achieved by modifying and improving the chemical and mechanical properties of solid–solid interfaces so that the ion-transfer and electron transfer can result in less undesired interfacial restructuring. Of these interfaces, we only review limited examples, and in most cases, these interfacial processes are coupled together, and complicated changes are induced at electrode–electrolyte interfaces. Besides reviewing what occurs at these interfaces, we also discuss strategies to modify the interfaces for desired properties. In addition, we emphasize the importance of *in situ* and *operando* characterization methods, particularly synchrotron X-ray techniques, in understanding these interfacial processes during the operation of the electrochemical energy systems. The goal of future studies of complex interfacial processes is to establish a clear structure–property relationship that can link changes at the electrode–electrolyte interfaces to the overall performance at the device level, thus providing guidance to advance the technology of electrochemical energy storage and conversion systems to meet the requirements of society development.

Conflicts of interest

There are no conflicts to declare.

Acknowledgements

This work was supported by the National Science Foundation under Grant No. CBET-1949870, CBET-2016192, NNCI-2025489, and DMR-1832803.

 This journal is © The Royal Society of Chemistry 2021

References

1 J. Xiao, *Science*, 2019, **366**, 426–427.
2 H. Tian, Z. Li, G. Feng, Z. Yang, D. Fox, M. Wang, H. Zhou, L. Zhai, A. Kushima, Y. Du, Z. Feng, X. Shan and Y. Yang, *Nat. Commun.*, 2021, **12**, 237.
3 J. Yue, X. Y. Zhu, F. D. Han, X. L. Fan, L. N. Wang, J. Yang and C. S. Wang, *ACS Appl. Mater. Interfaces*, 2018, **10**, 39645–39650.
4 M. Y. Wang, B. H. Han, J. J. Deng, Y. Jiang, M. Y. Zhou, M. Lucero, Y. Wang, Y. B. Chen, Z. Z. Yang, A. T. N'Diaye, Q. Wang, Z. C. J. Xu and Z. X. Feng, *ACS Appl. Mater. Interfaces*, 2019, **11**, 5682–5686.
5 Z. Weng, J. B. Jing, Y. S. Wu, Z. S. Wu, X. T. Guo, K. L. Materna, W. Liu, V. S. Batista, G. W. Brudvig and H. L. Wang, *J. Am. Chem. Soc.*, 2016, **138**, 8076–8079.
6 S. Qiu, X. Y. Wu, M. Y. Wang, M. Lucero, Y. Wang, J. Wang, Z. Z. Yang, W. Q. Xu, Q. Wang, M. Gu, J. G. Wen, Y. Q. Huang, Z. C. J. Xu and Z. X. Feng, *Nano Energy*, 2019, **64**, 103941.
7 G. M. Rupp, A. K. Opitz, A. Nenning, A. Limbeck and J. Fleig, *Nat. Mater.*, 2017, **16**, 640–650.
8 P. X. Bai, Y. W. He, P. X. Xiong, X. X. Zhao, K. Xu and Y. H. Xu, *Energy Storage Mater.*, 2018, **13**, 274–282.
9 D. D. Wang, Q. Z. Yan, M. Q. Li, H. P. Gao, J. H. Tian, Z. Q. Shan, N. Wang, J. Luo, M. Zhou and Z. Chen, *Nanoscale*, 2021, **13**, 2811–2819.
10 A. Friesen, S. Hildebrand, F. Horsthemke, M. Borner, R. Klopsch, P. Niehoff, F. M. Schappacher and M. Winter, *J. Power Sources*, 2017, **363**, 70–77.
11 J. Y. Wang, W. Huang, A. Pei, Y. Z. Li, F. F. Shi, X. Y. Yu and Y. Cui, *Nat. Energy*, 2019, **4**, 664–670.
12 S. Y. Luchkin, S. A. Lipovskikh, N. S. Katorova, A. A. Savina, A. M. Abakumov and K. J. Stevenson, *Sci. Rep.*, 2020, **10**, 8550.
13 L. M. Suo, D. Oh, Y. X. Lin, Z. Q. Zhuo, O. Borodin, T. Gao, F. Wang, A. Kushima, Z. Q. Wang, H. C. Kim, Y. Qi, W. L. Yang, F. Pan, J. Li, K. Xu and C. S. Wang, *J. Am. Chem. Soc.*, 2017, **139**, 18670–18680.
14 K. Macounova, M. Makarova, J. Franc, J. Jirkovsky and P. Krtil, *Electrochem. Solid-State Lett.*, 2008, **11**, F27–F29.
15 Y. Duan, S. N. Sun, S. B. Xi, X. Ren, Y. Zhou, G. L. Zhang, H. T. Yang, Y. H. Du and Z. C. J. Xu, *Chem. Mater.*, 2017, **29**, 10534–10541.
16 M. Wang, B. Han, J. Deng, Y. Jiang, M. Zhou, M. Lucero, Y. Wang, Y. Chen, Z. Yang, A. T. N'Diaye, Q. Wang, Z. J. Xu and Z. Feng, *ACS Appl. Mater. Interfaces*, 2019, **11**, 5682–5686.
17 Z. L. Wang, D. Xu, J. J. Xu and X. B. Zhang, *Chem. Soc. Rev.*, 2014, **43**, 7746–7786.
18 Y. Y. Zhang, H. W. Lei, D. L. Duan, E. Villota, C. Liu and R. Ruan, *ACS Appl. Mater. Interfaces*, 2018, **10**, 20429–20439.
19 P. Y. Wang, M. Y. Yan, J. S. Meng, G. P. Jiang, L. B. Qu, X. L. Pan, J. Z. Liu and L. Q. Mai, *Nat. Commun.*, 2017, **8**, 645.
20 J. Tymoczko, F. Calle-Vallejo, V. Colic, M. T. M. Koper, W. Schuhmann and A. S. Bandarenka, *ACS Catal.*, 2014, **4**, 3772–3778.
21 W. T. Hong, K. A. Stoerzinger, Y. L. Lee, L. Giordano, A. Grimaud, A. M. Johnson, J. Hwang, E. J. Crumlin, W. L. Yang and Y. Shao-Horn, *Energy Environ. Sci.*, 2017, **10**, 2190–2200.
22 F. Wang, O. Borodin, M. S. Ding, M. Gobet, J. Vatamanu, X. L. Fan, T. Gao, N. Eidson, Y. J. Liang, W. Sun, S. Greenbaum, K. Xu and C. S. Wang, *Joule*, 2018, **2**, 2178.
23 J. Asenbauer, T. Eisenmann, M. Kuenzel, A. Kazzazi, Z. Chen and D. Bresser, *Sustainable Energy Fuels*, 2020, **4**, 5387–5416.
24 M. Agostini, B. Scrosati and J. Hassoun, *Adv. Energy Mater.*, 2015, **5**, 1500481.
25 L. M. Suo, O. Borodin, T. Gao, M. Olguin, J. Ho, X. L. Fan, C. Luo, C. S. Wang and K. Xu, *Science*, 2015, **350**, 938–943.
26 X. Q. Zhang, M. F. Dong, Y. L. Xiong, Z. G. Hou, H. S. Ao, M. K. Liu, Y. C. Zhu and Y. T. Qian, *Small*, 2020, **16**, 2003585.
27 X. T. Xi, W. H. Li, B. H. Hou, Y. Yang, Z. Y. Gu and X. L. Wu, *ACS Appl. Energy Mater.*, 2019, **2**, 201–206.
28 K. A. Stoerzinger, M. Favaro, P. N. Ross, Z. Hussain, Z. Liu, J. Yano and E. J. Crumlin, *Top. Catal.*, 2018, **61**, 2152–2160.
29 A. J. Tkalych, H. L. L. Zhuang and E. A. Carter, *ACS Catal.*, 2017, **7**, 5329–5339.
30 H. Ali-Loytty, M. W. Louie, M. R. Singh, L. Li, H. G. S. Casalongue, H. Ogasawara, E. J. Crumlin, Z. Liu, A. T. Bell, A. Nilsson and D. Friebel, *J. Phys. Chem. C*, 2016, **120**, 2247–2253.
31 B. R. Wygant, K. Kawashima and C. B. Mullins, *ACS Energy Lett.*, 2018, **3**, 2956–2966.
32 S. T. Christensen, B. Lee, Z. X. Feng, M. C. Hersam and M. J. Bedzyk, *Appl. Surf. Sci.*, 2009, **256**, 423–427.
33 S. T. Christensen, J. W. Elam, B. Lee, Z. Feng, M. J. Bedzyk and M. C. Hersam, *Chem. Mater.*, 2009, **21**, 516–521.
34 Z. Li, S. F. Ji, Y. W. Liu, X. Cao, S. B. Tian, Y. J. Chen, Z. G. Niu and Y. D. Li, *Chem. Rev.*, 2020, **120**, 623–682.
35 G. A. Somorjai and Y. Li, *Introduction to surface chemistry and catalysis*, Wiley, Hoboken, NJ, 2nd edn, 2010.
36 J. M. Dreimann, E. Kohls, H. F. W. Warmeling, M. Stein, L. F. Guo, M. Garland, T. N. Dinh and A. J. Vorholt, *ACS Catal.*, 2019, **9**, 4308–4319.
37 C. Barroo, Z. J. Wang, R. Schloegl and M. G. Willinger, *Nat. Catal.*, 2020, **3**, 30–39.
38 Z. Feng, Q. Ma, J. Lu, H. Feng, J. W. Elam, P. C. Stair and M. J. Bedzyk, *RSC Adv.*, 2015, **5**, 103834–103840.
39 H. J. Freund and G. Pacchioni, *Chem. Soc. Rev.*, 2008, **37**, 2224–2242.
40 H. J. Freund, *Surf. Sci.*, 2002, **500**, 271–299.
41 M. Baumer and H. J. Freund, *Prog. Surf. Sci.*, 1999, **61**, 127–198.
42 B. J. Xu, X. Y. Liu, J. Haubrich and C. M. Friend, *Nat. Chem.*, 2010, **2**, 61–65.
43 B. C. Wiegand and C. M. Friend, *Chem. Rev.*, 1992, **92**, 491–504.
44 B. K. Min and C. M. Friend, *Chem. Rev.*, 2007, **107**, 2709–2724.
45 Z. Feng, M. E. McBriarty, A. U. Mane, J. Lu, P. C. Stair, J. W. Elam and M. J. Bedzyk, *RSC Adv.*, 2014, **4**, 64608–64616.
46 Z. X. Feng, J. L. Lu, H. Feng, P. C. Stair, J. W. Elam and M. J. Bedzyk, *J. Phys. Chem. Lett.*, 2013, **4**, 285–291.
47 Z. X. Feng, L. Cheng, C. Y. Kim, J. W. Elam, Z. Zhang, L. A. Curtiss, P. Zapol and M. J. Bedzyk, *J. Phys. Chem. Lett.*, 2012, **3**, 2845–2850.
48 Z. X. Feng, S. T. Christensen, J. W. Elam, B. Lee, M. C. Hersam and M. J. Bedzyk, *J. Appl. Phys.*, 2011, **110**, 102202.
49 Z. X. Feng, A. Kazimirov and M. J. Bedzyk, *ACS Nano*, 2011, **5**, 9755–9760.
50 Z. X. Feng, C. Y. Kim, J. W. Elam, Q. Ma, Z. Zhang and M. J. Bedzyk, *J. Am. Chem. Soc.*, 2009, **131**, 18200.
51 A. Berenov, A. Atkinson, J. Kilner, M. Ananyev, V. Eremin, N. Porotnikova, A. Farlenkov, E. Kurumchin, H. J. M. Bouwmeester, E. Bucher and W. Sitte, *Solid State Ionics*, 2014, **268**, 102–109.
52 W. Lee, H. J. Jung, M. H. Lee, Y. B. Kim, J. S. Park, R. Sinclair and F. B. Prinz, *Adv. Funct. Mater.*, 2012, **22**, 965–971.
53 S. Hong, H. Yang, Y. Lim, F. B. Prinz and Y. B. Kim, *ACS Appl. Mater. Interfaces*, 2019, **11**, 41338–41346.
54 M. Kubicek, Z. H. Cai, W. Ma, B. Yildiz, H. Hutter and J. Fleig, *ACS Nano*, 2013, **7**, 3276–3286.
55 F. F. Dong, Y. B. Chen, D. J. Chen and Z. P. Shao, *ACS Appl. Mater. Interfaces*, 2014, **6**, 11180–11189.
56 S. B. Adler, J. A. Lane and B. C. H. Steele, *J. Electrochem. Soc.*, 1996, **143**, 3554–3564.
57 S. B. Adler, *Solid State Ionics*, 1998, **111**, 125–134.
58 W. C. Chueh and S. M. Haile, *Annu. Rev. Chem. Biomol. Eng.*, 2012, **3**, 313–341.
59 S. L. Pang, G. M. Yang, X. N. Jiang, X. Q. Shen, D. W. Rao and C. L. Chen, *J. Catal.*, 2020, **381**, 408–414.
60 G. M. Yang, W. Zhou, M. L. Liu and Z. P. Shao, *ACS Appl. Mater. Interfaces*, 2016, **8**, 35308–35314.
61 E. Mutoro, E. J. Crumlin, M. D. Biegalski, H. M. Christen and Y. Shao-Horn, *Energy Environ. Sci.*, 2011, **4**, 3689–3696.
62 Z. L. Jian, W. T. Wang, M. Y. Wang, Y. Wang, N. AuYeung, M. Liu and Z. X. Feng, *Chin. Chem. Lett.*, 2018, **29**, 1768–1772.
63 G. J. La O', S. J. Ahn, E. Crumlin, Y. Orikasa, M. D. Biegalski, H. M. Christen and Y. Shao-Horn, *Angew. Chem., Int. Ed.*, 2010, **49**, 5344–5347.
64 E. J. Crumlin, E. Mutoro, Z. Liu, M. E. Grass, M. D. Biegalski, Y. L. Lee, D. Morgan, H. M. Christen, H. Bluhm and Y. Shao-Horn, *Energy Environ. Sci.*, 2012, **5**, 6081–6088.
65 C. R. Kreller, T. J. McDonald, S. B. Adler, E. J. Crumlin, E. Mutoro, S. J. Ahn, G. J. La O', Y. Shao-Horn, M. D. Biegalski, H. M. Christen, R. R. Chater and J. A. Kilner, *J. Electrochem. Soc.*, 2013, **160**, F931–F942.
66 T. C. Geary, D. Lee, Y. Shao-Horn and S. B. Adler, *J. Electrochem. Soc.*, 2016, **163**, F1107–F1114.
67 Z. X. Feng, Y. Yacoby, M. J. Gadre, Y. L. Lee, W. T. Hong, H. Zhou, M. D. Biegalski, H. M. Christen, S. B. Adler, D. Morgan and Y. Shao-Horn, *J. Phys. Chem. Lett.*, 2014, **5**, 1027–1034.

68 E. Mutoro, E. J. Crumlin, H. Popke, B. Luerssen, M. Amati, M. K. Abyaneh, M. D. Biegalski, H. M. Christen, L. Gregoratti, J. Janek and Y. Shao-Horn, *J. Phys. Chem. Lett.*, 2012, **3**, 40–44.
69 Z. X. Feng, E. J. Crumlin, W. T. Hong, D. Lee, E. Mutoro, M. D. Biegalski, H. Zhou, H. Bluhm, H. M. Christen and Y. Shao-Horn, *J. Phys. Chem. Lett.*, 2013, **4**, 1512–1518.
70 M. Li, M. H. Zheng, B. B. Hu, Y. X. Zhang and C. R. Xia, *Electrochim. Acta*, 2017, **230**, 196–203.
71 X. Xu, C. Wang, M. Fronzi, X. Liu, L. Bi and X. S. Zhao, *Mater. Renew. Sustain. Energy*, 2019, **8**, 15.
72 Y. Chen, A. Hinerman, L. Liang, K. Gerdes, S. P. Navia, J. Prucz and X. Y. Song, *J. Power Sources*, 2018, **405**, 45–50.
73 J. D. Fehribach and R. O'Hayre, *SIAM J. Appl. Math.*, 2009, **70**, 510–530.
74 Y. Yan, S. C. Sandu, J. Conde and P. Muralt, *J. Power Sources*, 2012, **206**, 84–90.
75 M. H. Wu, J. L. Huang, K. Z. Fung and D. F. Lii, *Surf. Coat. Technol.*, 2010, **205**, 30–34.
76 T. M. M. Heenan, J. J. Bailey, X. Lu, J. B. Robinson, F. Iacoviello, D. P. Finegan, D. J. L. Brett and P. R. Shearing, *Fuel Cells*, 2017, **17**, 75–82.
77 S. Ricciardi, J. C. Ruiz-Morales and P. Nunez, *Solid State Ionics*, 2009, **180**, 1083–1090.
78 S. Zhang and A. M. Gokhale, *J. Power Sources*, 2012, **219**, 172–179.
79 G. F. Cai, Y. L. Zhang, H. L. Dai, S. C. He, L. Ge, H. Chen and L. C. Guo, *Mater. Lett.*, 2017, **195**, 232–235.
80 W. Jeong, W. Yu, M. S. Lee, S. J. Bai, G. Y. Cho and S. W. Cha, *Int. J. Hydrogen Energy*, 2020, **45**, 32442–32448.
81 N. Vivet, S. Chupin, E. Estrade, A. Richard, S. Bonnamy, D. Rochais and E. Bruneton, *J. Power Sources*, 2011, **196**, 9989–9997.
82 Y. Chen, Z. H. Cai, Y. Kuru, W. Ma, H. L. Tuller and B. Yildiz, *Adv. Energy Mater.*, 2013, **3**, 1221–1229.
83 Z. X. Feng, Y. Yacoby, W. T. Hong, H. Zhou, M. D. Biegalski, H. M. Christen and Y. Shao-Horn, *Energy Environ. Sci.*, 2014, **7**, 1166–1174.
84 Y.-L. Lee, J. Kleis, J. Rossmeisl, Y. Shao-Horn and D. Morgan, *Energy Environ. Sci.*, 2011, **4**, 3966–3970.
85 Y. L. Lee, J. Kleis, J. Rossmeisl and D. Morgan, *Phys. Rev. B: Condens. Matter Mater. Phys.*, 2009, **80**, 224101.
86 J. Hwang, Z. X. Feng, N. Charles, X. R. Wang, D. Lee, K. A. Stoerzinger, S. Muy, R. R. Rao, D. Lee, R. Jacobs, D. Morgan and Y. Shao-Horn, *Mater. Today*, 2019, **31**, 100–118.
87 J. Hwang, K. Akkiraju, J. Corchado-Garcia and Y. Shao-Horn, *J. Phys. Chem. C*, 2019, **123**, 24469–24476.
88 Y. Chen, D. D. Fong, F. W. Herbert, J. Rault, J. P. Rueff, N. Tsvetkov and B. Yildiz, *Chem. Mater.*, 2018, **30**, 3359–3371.
89 X. F. Yang, J. Hu, J. Fu, R. Q. Wu and B. E. Koel, *Angew. Chem., Int. Ed.*, 2011, **50**, 10182–10185.
90 H. Y. Zhu, S. Zhang, D. Su, G. M. Jiang and S. H. Sun, *Small*, 2015, **11**, 3545–3549.
91 Y. Jiao, Y. Zheng, M. T. Jaroniec and S. Z. Qiao, *Chem. Soc. Rev.*, 2015, **44**, 2060–2086.
92 S. Ko, Y. Yamada and A. Yamada, *ACS Appl. Mater. Interfaces*, 2019, **11**, 45554–45560.
93 H. T. Zhang, D. Y. Wang and C. Shen, *Appl. Surf. Sci.*, 2020, **507**, 145059.
94 B. Hammer and J. K. Norskov, *Adv. Catal.*, 2000, **45**, 71–129.
95 J. K. Norskov, J. Rossmeisl, A. Logadottir, L. Lindqvist, J. R. Kitchin, T. Bligaard and H. Jonsson, *J. Phys. Chem. B*, 2004, **108**, 17886–17892.
96 Z. Y. Duan and G. F. Wang, *J. Phys. Chem. C*, 2013, **117**, 6284–6292.
97 J. Greeley, I. E. L. Stephens, A. S. Bondarenko, T. P. Johansson, H. A. Hansen, T. F. Jaramillo, J. Rossmeisl, I. Chorkendorff and J. K. Norskov, *Nat. Chem.*, 2009, **1**, 552–556.
98 C. Chen, Y. J. Kang, Z. Y. Huo, Z. W. Zhu, W. Y. Huang, H. L. L. Xin, J. D. Snyder, D. G. Li, J. A. Herron, M. Mavrikakis, M. F. Chi, K. L. More, Y. D. Li, N. M. Markovic, G. A. Somorjai, P. D. Yang and V. R. Stamenkovic, *Science*, 2014, **343**, 1339–1343.
99 R. R. Rao, M. J. Kolb, N. B. Halck, A. F. Pedersen, A. Mehta, H. You, K. A. Stoerzinger, Z. X. Feng, H. A. Hansen, H. Zhou, L. Giordano, J. Rossmeisl, T. Vegge, I. Chorkendorff, I. E. L. Stephens and Y. Shao-Horn, *Energy Environ. Sci.*, 2017, **10**, 2626–2637.
100 R. R. Rao, M. J. Kolb, J. Hwang, A. F. Pedersen, A. Mehta, H. You, K. A. Stoerzinger, Z. X. Feng, H. Zhou, H. Bluhm, L. Giordano, I. E. L. Stephens and Y. Shao-Horn, *J. Phys. Chem. C*, 2018, **122**, 17802–17811.
101 N. Alonso-Vante, P. Borthen, M. Fieber-Erdmann, H. H. Strehblow and E. Holub-Krappe, *Electrochim. Acta*, 2000, **45**, 4227–4236.
102 D. Y. Kuo, J. K. Kawasaki, J. N. Nelson, J. Kloppenburg, G. Hautier, K. M. Shen, D. G. Schlom and J. Suntivich, *J. Am. Chem. Soc.*, 2017, **139**, 3473–3479.
103 J. J. Velasco-Velez, V. Pfeifer, M. Havecker, R. S. Weatherup, R. Arrigo, C. H. Chuang, E. Stotz, G. Weinberg, M. Salmeron, R. Schlogl and A. Knop-Gericke, *Angew. Chem., Int. Ed.*, 2015, **54**, 14554–14558.
104 H. F. Feng, X. Xu, Y. Du and S. X. Dou, *Electrochem. Energy Rev.*, 2021, 249–268.
105 J. H. Bang and H. Kim, *Bull. Korean Chem. Soc.*, 2011, **32**, 3660–3665.
106 L. Wang, Q. Zhou, Z. H. Pu, Q. Zhang, X. Q. Mu, H. Y. Jing, S. L. Liu, C. Y. Chen and S. C. Mu, *Nano Energy*, 2018, **53**, 270–276.
107 W. Z. Tu, K. Chen, L. J. Zhu, H. C. Zai, E. Bin, X. X. Ke, C. F. Chen, M. L. Sui, Q. Chen and Y. J. Li, *Adv. Funct. Mater.*, 2019, **29**, 1807070.
108 Y. Y. Li, X. C. Du, J. W. Huang, C. Y. Wu, Y. H. Sun, G. F. Zou, C. T. Yang and J. Xiong, *Small*, 2019, **15**, 1901980.
109 Y. F. Wang, D. Sun, M. Y. Wang, Z. X. Feng and A. S. Hall, *J. Phys. Chem. C*, 2020, **124**, 5220–5224.
110 Q. F. Gong, P. Ding, M. Q. Xu, X. R. Zhu, M. Y. Wang, J. Deng, Q. Ma, N. Han, Y. Zhu, J. Lu, Z. X. Feng, Y. F. Li, W. Zhou and Y. G. Li, *Nat. Commun.*, 2019, **10**, 2807.
111 X. Zhang, Y. Wang, M. Gu, M. Y. Wang, Z. S. Zhang, W. Y. Pan, Z. Jiang, H. Z. Zheng, M. Lucero, H. L. Wang, G. E. Sterbinsky, Q. Ma, Y. G. Wang, Z. X. Feng, J. Li, H. J. Dai and Y. Y. Liang, *Nat. Energy*, 2020, **5**, 684–692.
112 Y. S. Wu, J. B. Jiang, Z. Weng, M. Y. Wang, D. L. J. Broere, Y. R. Zhong, G. W. Brudvig, Z. X. Feng and H. L. Wang, *ACS Cent. Sci.*, 2017, **3**, 847–852.
113 G. Y. Chen, K. A. Kuttiyiel, M. Li, D. Su, L. Du, C. Y. Du, Y. Z. Gao, W. D. Fei, G. P. Yin, K. Sasaki and R. R. Adzic, *J. Mater. Chem. A*, 2018, **6**, 20725–20736.
114 R. Majee, Q. A. Islam, S. Mondal and S. Bhattacharyya, *Chem. Sci.*, 2020, **11**, 10180–10189.
115 C. W. Tung, Y. Y. Hsu, Y. P. Shen, Y. X. Zheng, T. S. Chan, H. S. Sheu, Y. C. Cheng and H. M. Chen, *Nat. Commun.*, 2015, **6**, 8106.
116 C. Wei, Z. X. Feng, G. G. Scherer, J. Barber, Y. Shao-Horn and Z. C. J. Xu, *Adv. Mater.*, 2017, **29**, 1606800.
117 C. Wei, Z. X. Feng, M. Baisariyev, L. H. Yu, L. Zeng, T. P. Wu, H. Y. Zhao, Y. Q. Huang, M. J. Bedzyk, T. Sritharan and Z. C. J. Xu, *Chem. Mater.*, 2016, **28**, 4129–4133.
118 Z. Weng, Y. S. Wu, M. Y. Wang, J. B. Jiang, K. Yang, S. J. Huo, X. F. Wang, Q. Ma, G. W. Brudvig, V. S. Batista, Y. Y. Liang, Z. X. Feng and H. L. Wang, *Nat. Commun.*, 2018, **9**, 415.
119 J. Suntivich, K. J. May, H. A. Gasteiger, J. B. Goodenough and Y. Shao-Horn, *Science*, 2011, **334**, 1383–1385.
120 K. J. May, C. E. Carlton, K. A. Stoerzinger, M. Risch, J. Suntivich, Y. L. Lee, A. Grimaud and Y. Shao-Horn, *J. Phys. Chem. Lett.*, 2012, **3**, 3264–3270.
121 L. C. Seitz, C. F. Dickens, K. Nishio, Y. Hikita, J. Montoya, A. Doyle, C. Kirk, A. Vojvodic, H. Y. Hwang, J. K. Norskov and T. F. Jaramillo, *Science*, 2016, **353**, 1011–1014.
122 G. Wan, J. W. Freeland, J. Kloppenburg, G. Petretto, J. N. Nelson, D. Y. Kuo, C. J. Sun, J. G. Wen, J. T. Diulus, G. S. Herman, Y. Q. Dong, R. H. Kou, J. Y. Sun, S. Chen, K. M. Shen, D. G. Schlom, G. M. Rignanese, G. Hautier, D. D. Fong, Z. X. Feng, H. Zhou and J. Suntivich, *Sci. Adv.*, 2021, **7**, eabc7323.
123 P. S. Li, M. Y. Wang, X. X. Duan, L. R. Zheng, X. P. Cheng, Y. F. Zhang, Y. Kuang, Y. P. Li, Q. Ma, Z. X. Feng, W. Liu and X. M. Sun, *Nat. Commun.*, 2019, **10**, 1711.
124 Z. Cai, D. J. Zhou, M. Y. Wang, S. M. Bak, Y. S. Wu, Z. S. Wu, Y. Tian, X. Y. Xiong, Y. P. Li, W. Liu, S. Siahrostami, Y. Kuang, X. Q. Yang, H. H. Duan, Z. X. Feng, H. L. Wang and X. M. Sun, *Angew. Chem., Int. Ed.*, 2018, **57**, 9392–9396.
125 C. Cai, M. Y. Wang, S. B. Han, Q. Wang, Q. Zhang, Y. M. Zhu, X. M. Yang, D. J. Wu, X. T. Zu, G. E. Sterbinsky, Z. X. Feng and M. Gu, *ACS Catal.*, 2021, **11**, 123–130.

 This journal is © The Royal Society of Chemistry 2021

126 C. Hu, E. H. Song, M. Y. Wang, W. Chen, F. Q. Huang, Z. X. Feng, J. J. Liu and J. C. Wang, *Adv. Sci.*, 2021, **8**, 2001881.
127 M. Y. Wang, L. Arnadottir, Z. C. J. Xu and Z. X. Feng, *Nano-Micro Lett.*, 2019, **11**, 47.
128 Y. Zhao, X. Tan, W. F. Yang, C. Jia, X. J. Chen, W. H. Ren, S. C. Smith and C. Zhao, *Angew. Chem., Int. Ed.*, 2020, **59**, 21493–21498.
129 S. H. Lee, J. C. Lin, M. Farmand, A. T. Landers, J. T. Feaster, J. E. A. Acosta, J. W. Beeman, Y. F. Ye, J. Yano, A. Mehta, R. C. Davis, T. F. Jaramillo, C. Hahn and W. S. Drisdell, *J. Am. Chem. Soc.*, 2021, **143**, 588–592.
130 S. Verma, X. Lu, S. C. Ma, R. I. Masel and P. J. A. Kenis, *Phys. Chem. Chem. Phys.*, 2016, **18**, 7075–7084.
131 Y. P. Wijaya, K. J. Smith, C. S. Kim and E. L. Gyenge, *J. Appl. Electrochem.*, 2021, **51**, 51–63.
132 G. F. Li, M. Divinagracia, M. F. Labata, J. D. Ocon and P. Y. A. Chuang, *ACS Appl. Mater. Interfaces*, 2019, **11**, 33748–33758.
133 J. A. Arminio-Ravelo, A. W. Jensen, K. D. Jensen, J. Quinson and M. Escudero-Escribano, *ChemPhysChem*, 2019, **20**, 2956–2963.
134 A. C. Garcia and M. T. M. Koper, *ACS Catal.*, 2018, **8**, 9359–9363.
135 V. Colic, M. D. Pohl, D. Scieszka and A. S. Bandarenka, *Catal. Today*, 2016, **262**, 24–35.
136 M. M. Waegele, C. M. Gunathunge, J. Y. Li and X. Li, *J. Chem. Phys.*, 2019, **151**, 160902.
137 C. Y. Yang, J. Chen, T. T. Qing, X. L. Fan, W. Sun, A. von Cresce, M. S. Ding, O. Borodin, J. Vatamanu, M. A. Schroeder, N. Eidson, C. S. Wang and K. Xu, *Joule*, 2017, **1**, 122–132.
138 F. Zhang, B. Ji, X. F. Tong, M. H. Sheng, X. L. Zhang, C. S. Lee and Y. B. Tang, *Adv. Mater. Interfaces*, 2016, **3**, 1600605.
139 S. Komaba, W. Murata, T. Ishikawa, N. Yabuuchi, T. Ozeki, T. Nakayama, A. Ogata, K. Gotoh and K. Fujiwara, *Adv. Funct. Mater.*, 2011, **21**, 3859–3867.
140 N. Liu, Z. D. Lu, J. Zhao, M. T. McDowell, H. W. Lee, W. T. Zhao and Y. Cui, *Nat. Nanotechnol.*, 2014, **9**, 187–192.
141 Y. Shi, Z. B. Yi, Y. P. Kuang, H. Y. Guo, Y. Z. Li, C. Liu and Z. G. Lu, *Chem. Commun.*, 2020, **56**, 11613–11616.
142 C. X. Xu and J. J. Jiang, *Rare Met.*, 2021, **40**, 243–245.
143 Z. B. Yi, Y. Liu, Y. Z. Li, L. J. Zhou, Z. Y. Wang, J. Q. Zhang, H. Cheng and Z. G. Lu, *Small*, 2020, **16**, 1905301.
144 L. J. Chen, K. M. Song, J. Shi, J. Y. Zhang, L. W. Mi, W. H. Chen, C. T. Liu and C. Y. Shen, *Sci. China Mater.*, 2021, **64**, 105–114.
145 Q. M. Gan, H. N. He, Y. H. Zhu, Z. Y. Wang, N. Qin, S. Gu, Z. Q. Li, W. Luo and Z. G. Lu, *ACS Nano*, 2019, **13**, 9247–9258.
146 X. Lian, Z. R. Ma, Z. H. Zhang, J. L. Yang, S. Sun, C. D. Gu, Y. Liu, H. H. Ding, J. Hu, X. Cao, J. F. Zhu, S. Z. Li and W. Chen, *Nano Res.*, 2020, **13**, 3224–3229.
147 M. Favaro, J. H. Yang, S. Nappini, E. Magnano, F. M. Toma, E. J. Crumlin, J. Yano and I. D. Sharp, *J. Am. Chem. Soc.*, 2017, **139**, 8960–8970.
148 P. Munster, A. Heckmann, R. Nolle, M. Winter, K. Beltrop and T. Placke, *Batteries Supercaps*, 2019, **2**, 992–1006.
149 S. H. Kim, Y. S. Kim, W. J. Baek, S. Heo, S. Han and H. Jung, *J. Power Sources*, 2018, **407**, 1–5.
150 W. Lu, J. S. Zhang, J. J. Xu, X. D. Wu and L. W. Chen, *ACS Appl. Mater. Interfaces*, 2017, **9**, 19313–19318.
151 X. F. Wang, Y. J. Li and Y. S. Meng, *Joule*, 2018, **2**, 2225–2234.
152 X. F. Wang, M. H. Zhang, J. Alvarado, S. Wang, M. Sina, B. Y. Lu, J. Bouwer, W. Xu, J. Xiao, J. G. Zhang, J. Liu and Y. S. Meng, *Nano Lett.*, 2017, **17**, 7606–7612.
153 Y. Z. Li, Y. B. Li, A. L. Pei, K. Yan, Y. M. Sun, C. L. Wu, L. M. Joubert, R. Chin, A. L. Koh, Y. Yu, J. Perrino, B. Butz, S. Chu and Y. Cui, *Science*, 2017, **358**, 506–510.
154 Z. Shadike, H. Lee, O. Borodin, X. Cao, X. L. Fan, X. L. Wang, R. Q. Lin, S. M. Bak, S. Ghose, K. Xu, C. S. Wang, J. Liu, J. Xiao, X. Q. Yang and E. Y. Hu, *Nat. Nanotechnol.*, 2021, 549–554.
155 J. Yu, C. Mu, X. Y. Qin, C. Shen, B. Y. Yan, H. G. Xue and H. Pang, *Adv. Mater. Interfaces*, 2017, **4**, 1700279.
156 X. Q. Shan, D. S. Charles, Y. K. Lei, R. M. Qiao, G. F. Wang, W. L. Yang, M. Feygenson, D. Su and X. W. Teng, *Nat. Commun.*, 2016, **7**, 13370.
157 S. Rothermel, P. Meister, G. Schmuelling, O. Fromm, H. W. Meyer, S. Nowak, M. Winter and T. Placke, *Energy Environ. Sci.*, 2014, **7**, 3412–3423.
158 Z. W. Zhang, J. L. Yang, W. Huang, H. S. Wang, W. J. Zhou, Y. B. Li, Y. Z. Li, J. W. Xu, W. X. Huang, W. Chiu and Y. Cui, *Matter*, 2021, **4**, 302–312.
159 W. Liu, X. F. Li, D. B. Xiong, Y. C. Hao, J. W. Li, H. R. Kou, B. Yan, D. J. Li, S. G. Lu, A. Koo, K. Adair and X. L. Sun, *Nano Energy*, 2018, **44**, 111–120.
160 S. C. Jung and Y. K. Han, *J. Phys. Chem. Lett.*, 2013, **4**, 2681–2685.
161 S. Neudeck, A. Mazilkin, C. Reitz, P. Hartmann, J. Janek and T. Brezesinski, *Sci. Rep.*, 2019, **9**, 5328.
162 X. Chen, M. Voros, J. C. Garcia, T. T. Fister, D. B. Buchholz, J. Franklin, Y. G. Du, T. C. Droubay, Z. X. Feng, H. Iddir, L. A. Curtiss, M. J. Bedzyk and P. Fenter, *ACS Appl. Energy Mater.*, 2018, **1**, 2526–2535.
163 Z. X. Feng, X. Chen, L. Qiao, A. L. Lipson, T. T. Fister, L. Zeng, C. Kim, T. H. Yi, N. Sa, D. L. Proffit, A. K. Burrell, J. Cabana, B. J. Ingram, M. D. Biegalski, M. J. Bedzyk and P. Fenter, *ACS Appl. Mater. Interfaces*, 2015, **7**, 28438–28443.
164 Z. X. Feng, X. Chen, T. T. Fister, M. J. Bedzyk and P. Fenter, *J. Appl. Phys.*, 2016, **120**, 015307.
165 X. F. He, Y. Z. Zhu and Y. F. Mo, *Nat. Commun.*, 2017, **8**, 15893.
166 Y. H. Zhang, J. F. Qian, W. Xu, S. M. Russell, X. L. Chen, E. Nasybulin, P. Bhattacharya, M. H. Engelhard, D. H. Mei, R. G. Cao, F. Ding, A. V. Cresce, K. Xu and J. G. Zhang, *Nano Lett.*, 2014, **14**, 6889–6896.
167 Y. Li, D. X. Cao, W. Arnold, Y. Ren, C. Liu, J. B. Jasinski, T. Druffel, Y. Cao, H. L. Zhu and H. Wang, *Energy Storage Mater.*, 2020, **31**, 344–351.
168 Z. J. Ju, J. W. Nai, Y. Wang, T. F. Liu, J. H. Zheng, H. D. Yuan, O. W. Sheng, C. B. Jin, W. K. Zhang, Z. Jin, H. Tian, Y. J. Liu and X. Y. Tao, *Nat. Commun.*, 2020, **11**, 488.
169 T. Y. Wang, Y. B. Li, J. Q. Zhang, K. Yan, P. Jaumaux, J. Yang, C. Y. Wang, D. Shanmukaraj, B. Sun, M. Armand, Y. Cui and G. X. Wang, *Nat. Commun.*, 2020, **11**, 5429.
170 X. Y. Zhang, A. X. Wang, X. J. Liu and J. Y. Luo, *Acc. Chem. Res.*, 2019, **52**, 3223–3232.
171 J. M. He, C. Yang, X. Yang, L. L. Liu, J. H. Li, Q. Liu, L. Peng, X. R. Liu and M. N. Qu, *Appl. Surf. Sci.*, 2020, **532**, 147357.
172 H. Guzman, F. Zammillo, D. Roldan, C. Galletti, N. Russo and S. Hernandez, *Catalysts*, 2021, **11**, 482.
173 H. Cheng, W. Yuan and K. Scott, *J. Power Sources*, 2008, **183**, 678–681.
174 Z. J. Liang, Q. L. Zou, Y. Wang and Y. C. Lu, *Small Methods*, 2017, **1**, 170015.
175 E. Murawski, N. Kananizadeh, S. Lindsay, A. M. Rao and S. C. Popat, *J. Power Sources*, 2021, **481**, 228992.
176 I. Asano, Y. Hamano, S. Tsujimura, O. Shirai and K. Kano, *Electrochemistry*, 2012, **80**, 324–326.
177 V. Briega-Martos, G. A. B. Mello, R. M. Aran-Ais, V. Climent, E. Herrero and J. M. Feliu, *J. Electrochem. Soc.*, 2018, **165**, J3045–J3051.
178 V. Briega-Martos, E. Herrero and J. M. Feliu, *Electrochim. Acta*, 2017, **241**, 497–509.
179 S. Rojas-Carbonell, K. Artyushkova, A. Serov, C. Santoro, I. Matanovic and P. Atanassov, *ACS Catal.*, 2018, **8**, 3041–3053.
180 A. Schumpe, I. Adler and W. D. Deckwer, *Biotechnol. Bioeng.*, 1978, **20**, 145–150.
181 E. Narita, F. Lawson and K. N. Han, *Hydrometallurgy*, 1983, **10**, 21–37.
182 L. J. Su, L. Y. Liu, B. Liu, J. N. Meng and X. B. Yan, *iScience*, 2020, **23**, 100995.
183 W. Xing, G. Yin and J. Zhang, *Rotating Electrode Methods and Oxygen Reduction Electrocatalysts*, Elsevier Science, 2014.
184 F. S. Gittleson, R. E. Jones, D. K. Ward and M. E. Foster, *Energy Environ. Sci.*, 2017, **10**, 1167–1179.
185 Y. Kanzaki, K. Tokuda and S. Bruckenstein, *J. Electrochem. Soc.*, 2014, **161**, H770–H779.
186 Y. H. Shih, G. V. Sagar and S. D. Lin, *J. Phys. Chem. C*, 2008, **112**, 123–130.
187 P. Kubicek, *Collect. Czech. Chem. Commun.*, 1978, **43**, 535–544.
188 S. C. Xu, Y. Kim, D. Higgins, M. Yusuf, T. F. Jaramillo and F. B. Prinz, *Electrochim. Acta*, 2017, **255**, 99–108.
189 X. Y. Mao, C. Lin, G. W. Graham and R. J. Gorte, *ACS Catal.*, 2020, **10**, 8840–8849.

190 H. Kawasoko, T. Shirasawa, S. Shiraki, T. Suzuki, S. Kobayashi, K. Nishio, R. Shimizu and T. Hitosugi, *ACS Appl. Energy Mater.*, 2020, **3**, 1358–1363.
191 S. Shiraki, T. Shirasawa, T. Suzuki, H. Kawasoko, R. Shimizu and T. Hitosugi, *ACS Appl. Mater. Interfaces*, 2018, **10**, 41732–41737.
192 H. Kawasoko, S. Shiraki, T. Suzuki, R. Shimizu and T. Hitosugi, *ACS Appl. Mater. Interfaces*, 2018, **10**, 27498–27502.
193 Y. He, M. Gu, H. Y. Xiao, L. L. Luo, Y. Y. Shao, F. Gao, Y. G. Du, S. X. Mao and C. M. Wang, *Angew. Chem., Int. Ed.*, 2016, **55**, 6244–6247.
194 Y. Z. Zhu, X. F. He and Y. F. Mo, *J. Mater. Chem. A*, 2016, **4**, 3253–3266.
195 J. W. Ju, J. Ma, Y. T. Wang, Y. Y. Cui, P. X. Han and G. L. Cui, *Energy Storage Mater.*, 2019, **20**, 269–290.
196 N. C. Rosero-Navarro, R. Kajiura, A. Miura and K. Tadanaga, *ACS Appl. Energy Mater.*, 2020, **3**, 11260–11268.
197 F. Lv, Z. Y. Wang, L. Y. Shi, J. F. Zhu, K. Edstrom, J. Mindemark and S. Yuan, *J. Power Sources*, 2019, **441**, 227175.
198 D. P. Clark and R. E. Meredith, *Electrochem. Technol.*, 1967, **5**, 446.
199 F. J. Q. Cortes, J. A. Lewis, J. Tippens, T. S. Marchese and M. T. McDowell, *J. Electrochem. Soc.*, 2019, **167**, 050502.
200 J. Y. Yang, Z. H. Gao, T. Ferber, H. F. Zhang, C. Guhl, L. T. Yang, Y. Y. Li, Z. Deng, P. R. Liu, C. W. Cheng, R. C. Che, W. Jaegermann, R. Hausbrand and Y. H. Huang, *J. Mater. Chem. A*, 2020, **8**, 7828–7835.
201 H. H. Xu, P. H. Chien, J. J. Shi, Y. T. Li, N. Wu, Y. Y. Liu, Y. Y. Hu and J. B. Goodenough, *Proc. Natl. Acad. Sci. U. S. A.*, 2019, **116**, 18815–18821.
202 W. B. Zhang, T. Leichtweiss, S. P. Culver, R. Koerver, D. Das, D. A. Weber, W. G. Zeier and J. Janek, *ACS Appl. Mater. Interfaces*, 2017, **9**, 35888–35896.
203 X. G. Hao, Q. Zhao, S. M. Su, S. Q. Zhang, J. B. Ma, L. Shen, Q. P. Yu, L. Zhao, Y. Liu, F. Y. Kang and Y. B. He, *Adv. Energy Mater.*, 2019, **9**, 1901604.
204 B. B. Wu, S. Y. Wang, J. Lochala, D. Desrochers, B. Liu, W. Q. Zhang, J. H. Yang and J. Xiao, *Energy Environ. Sci.*, 2018, **11**, 1803–1810.
205 T. An, H. H. Jia, L. F. Peng and J. Xie, *ACS Appl. Mater. Interfaces*, 2020, **12**, 20563–20569.
206 D. X. Cao, X. Sun, Q. Li, A. Natan, P. Y. Xiang and H. L. Zhu, *Matter*, 2020, **3**, 57–94.
207 H. Liu, X. B. Cheng, J. Q. Huang, H. Yuan, Y. Lu, C. Yan, G. L. Zhu, R. Xu, C. Z. Zhao, L. P. Hou, C. X. He, S. Kaskel and Q. Zhang, *ACS Energy Lett.*, 2020, **5**, 833–843.
208 X. Zhang, S. Wang, C. J. Xue, C. Z. Xin, Y. H. Lin, Y. Shen, L. L. Li and C. W. Nan, *Adv. Mater.*, 2019, **31**, 1806082.
209 G. M. Hou, X. X. Ma, Q. D. Sun, Q. Ai, X. Y. Xu, L. N. Chen, D. P. Li, J. H. Chen, H. Zhong, Y. Li, Z. B. Xu, P. C. Si, J. K. Feng, L. Zhang, F. Ding and L. J. Ci, *ACS Appl. Mater. Interfaces*, 2018, **10**, 18610–18618.
210 M. Golozar, A. Paolella, H. Demers, S. Bessette, M. Lagace, P. Bouchard, A. Guerfi, R. Gauvin and K. Zaghib, *Commun. Chem.*, 2019, **2**, 131.
211 S. F. Wang, H. H. Xu, W. D. Li, A. Dolocan and A. Manthiram, *J. Am. Chem. Soc.*, 2018, **140**, 250–257.
212 Q. Zhao, P. Y. Chen, S. K. Li, X. T. Liu and L. A. Archer, *J. Mater. Chem. A*, 2019, **7**, 7823–7830.
213 S. F. Lou, F. Zhang, C. K. Fu, M. Chen, Y. L. Ma, G. P. Yin and J. J. Wang, *Adv. Mater.*, 2020, 2000721.
214 M. Le Granvalet-Mancini, T. Hanrath and D. Teeters, *Solid State Ionics*, 2000, **135**, 283–290.
215 N. L. Wu, Y. T. Weng, F. S. Li, N. H. Yang, C. L. Kuo and D. S. Li, *Prog. Nat. Sci.: Mater. Int.*, 2015, **25**, 563–571.
216 D. C. Zhang, L. Zhang, K. Yang, H. Q. Wang, C. Yu, D. Xu, B. Xu and L. M. Wang, *ACS Appl. Mater. Interfaces*, 2017, **9**, 36886–36896.
217 N. W. Li, Y. X. Yin, C. P. Yang and Y. G. Guo, *Adv. Mater.*, 2016, **28**, 1853–1858.
218 K. Thanner, A. Varzi, D. Buchholz, S. J. Sedlmaier and S. Passerini, *ACS Appl. Mater. Interfaces*, 2020, **12**, 32851–32862.
219 S. Wang, R. Fang, Y. Li, Y. Liu, C. Xin, F. H. Richter and C.-W. Nan, *J. Materiomics*, 2021, **7**, 209–218.
220 Y. F. Mo, S. P. Ong and G. Ceder, *Chem. Mater.*, 2012, **24**, 15–17.
221 M. R. Busche, D. A. Weber, Y. Schneider, C. Dietrich, S. Wenzel, T. Leichtweiss, D. Schroder, W. B. Zhang, H. Weigand, D. Walter, S. J. Sedlmaier, D. Houtarde, L. F. Nazar and J. Janek, *Chem. Mater.*, 2016, **28**, 6152–6165.
222 Y. Z. Zhu, X. F. He and Y. F. Mo, *ACS Appl. Mater. Interfaces*, 2015, **7**, 23685–23693.
223 S. Wenzel, S. Randau, T. Leichtweiss, D. A. Weber, J. Sann, W. G. Zeier and J. Janek, *Chem. Mater.*, 2016, **28**, 2400–2407.
224 T. Hakari, M. Nagao, A. Hayashi and M. Tatsumisago, *J. Power Sources*, 2015, **293**, 721–725.
225 S. Wenzel, T. Leichtweiss, D. Kruger, J. Sann and J. Janek, *Solid State Ionics*, 2015, **278**, 98–105.
226 C. Z. Sun, Y. D. Ruan, W. P. Zha, W. W. Li, M. L. Cai and Z. Y. Wen, *Mater. Horiz.*, 2020, **7**, 1667–1696.
227 M. Nagao, A. Hayashi and M. Tatsumisago, *Electrochemistry*, 2012, **80**, 734–736.
228 T. Ates, M. Keller, J. Kulisch, T. Adermann and S. Passerini, *Energy Storage Mater.*, 2019, **17**, 204–210.
229 F. J. Simon, M. Hanauer, A. Henss, F. H. Richter and J. Janek, *ACS Appl. Mater. Interfaces*, 2019, **11**, 42186–42196.
230 Y. H. Xiao, Y. Wang, S. H. Bo, J. C. Kim, L. J. Miara and G. Ceder, *Nat. Rev. Mater.*, 2020, 105–126.
231 Z. J. Bi, N. Zhao, L. N. Ma, Z. Q. Fu, F. F. Xu, C. S. Wang and X. X. Guo, *Chem. Eng. J.*, 2020, **387**, 124089.
232 K. H. Nie, Y. S. Hong, J. L. Qiu, Q. H. Li, X. Q. Yu, H. Li and L. Q. Chen, *Front. Chem.*, 2018, **6**, 00616.
233 A. Schwobel, W. Jaegermann and R. Hausbrand, *Solid State Ionics*, 2016, **288**, 224–228.
234 J. Song, S. Jacke, G. Cherkashinin, S. Schmid, Q. F. Dong, R. Hausbrand and W. Jaegermann, *Electrochem. Solid-State Lett.*, 2011, **14**, A189–A191.
235 Z. Y. Wang, D. Santhanagopalan, W. Zhang, F. Wang, H. L. L. Xin, K. He, J. C. Li, N. Dudney and Y. S. Meng, *Nano Lett.*, 2016, **16**, 3760–3767.
236 W. B. Zhang, F. H. Richter, S. P. Culver, T. Leichtweiss, J. G. Lozano, C. Dietrich, P. G. Bruce, W. G. Zeier and J. Janek, *ACS Appl. Mater. Interfaces*, 2018, **10**, 22226–22236.
237 M. F. Groh, M. J. Sullivan, M. W. Gaultois, O. Pecher, K. J. Griffith and C. P. Grey, *Chem. Mater.*, 2018, **30**, 5886–5895.
238 J. Auvergniot, A. Cassel, J. B. Ledeuil, V. Viallet, V. Seznec and R. Dedryvere, *Chem. Mater.*, 2017, **29**, 3883–3890.
239 A. Sakuda, A. Hayashi and M. Tatsumisago, *Chem. Mater.*, 2010, **22**, 949–956.
240 K. H. Kim, Y. Iriyama, K. Yamamoto, S. Kumazaki, T. Asaka, K. Tanabe, C. A. J. Fisher, T. Hirayama, R. Murugan and Z. Ogumi, *J. Power Sources*, 2011, **196**, 764–767.
241 Z. Z. Tong, S. B. Wang, Y. K. Liao, S. F. Hu and R. S. Liu, *ACS Appl. Mater. Interfaces*, 2020, **12**, 47181–47196.
242 K. Yoshima, Y. Harada and N. Takami, *J. Power Sources*, 2016, **302**, 283–290.
243 C. W. Wang, F. C. Ren, Y. Zhou, P. F. Yan, X. D. Zhou, S. J. Zhang, W. Liu, W. D. Zhang, M. H. Zou, L. Y. Zeng, X. Y. Yao, L. Huang, J. T. Li and S. G. Sun, *Energy Environ. Sci.*, 2021, **14**, 437–450.
244 H. Wang, M. Yu, Y. Wang, Z. X. Feng, Y. Q. Wang, X. J. Lu, J. L. Zhu, Y. Ren and C. D. Liang, *J. Power Sources*, 2018, **401**, 111–116.
245 M. Lucero, S. Qiu and Z. Feng, *Carbon Energy*, 2021, 563–580.

 This journal is © The Royal Society of Chemistry 2021